Computational Materials Science 230 (2023) 112508

Contents lists available at ScienceDirect

Computational Materials Science

journal homepage: www.elsevier.com/locate/commatsci

Full length article

Effect of a micro-scale dislocation pileup on the atomic-scale multi-variant phase transformation and twinning

Yipeng Peng [a,b], Rigelesaiyin Ji [c], Thanh Phan [d], Laurent Capolungo [b], Valery I. Levitas [d,e,f], Liming Xiong [a,d,*]

[a] Department of Mechanical and Aerospace Engineering, NC State University, Raleigh NC 27695, USA
[b] Materials Science and Technology Division, Los Alamos National Laboratory, Los Alamos NM 87545, USA
[c] 3MT Modeling and Simulation Group, Schlumberger, Sugar Land TX 77478, USA
[d] Department of Aerospace Engineering, Iowa State University, Ames IA 50011, USA
[e] Department of Mechanical Engineering, Iowa State University, Ames IA 50011, USA
[f] U.S. Department of Energy, Ames Laboratory, Ames IA 50011, USA

ARTICLE INFO

Dataset link: https://github.ncsu.edu/tphan4/CAC.git

Keywords:
Dislocations
Interface
Twinning
Phase transformation
Atomistic and multiscale simulations

ABSTRACT

In this paper, we perform concurrent atomistic–continuum (CAC) simulations to assess the contribution of the internal stress induced by the microscale dislocation pileup at an atomically structured interface to the atomic-scale phase transformations (PTs), reverse PTs, and twinning. The main novelty of this work is to unify the atomistic description of the interface and the coarse-grained (CG) description of the lagging dislocations away from the interface within one single framework. Our major findings are: **(a)** the interface dynamically responds to a pileup by forming steps/ledges, the height of which is proportional to the number of dislocations arriving at the interface; **(b)** the pileup-induced internal stress concentration profile follows neither the classical Eshelby model nor the super-dislocation model alone, but a combination of them; **(c)** when the pre-sheared sample is compressed, a direct square-to-hexagonal PT occurs ahead of the pileup tip and eventually grows into a wedge shape. The two variants of the hexagonal phases form a twin with respect to each other; **(d)** upon a further increase of the loading, part of the newly formed hexagonal phase transforms back to the square phase. The square product phase resulting from this reverse PT forms a twin with respect to the initial square phase. All phase boundaries (PBs) and twin boundaries (TBs) are stationary and correspond to zero thermodynamic Eshelby driving forces; and **(e)** the microscale dislocation pileup-induced internal shear stress and the structural change at the atomic-scale interface reduces the stress required for initiating a PT by a factor of 5.5, comparing with that in the sample containing no dislocations. This work is the first characterization of the behavior of PTs/twinning resulting from the reaction between a microscale dislocation slip and an atomically structured interface. The gained knowledge will advance our understanding of how the multi-phase material behaves in many complex physical processes, such as the synthesis of multi-phase high-entropy alloys or superhard ceramics under high-pressure torsion, deep mantle earthquakes in geophysics, and so on, which all involve dislocation slip, PTs, twinning, and their interactions across from the atomistic to the microscale and beyond.

1. Introduction

Dislocations, phase transformations (PTs), and twinning are three most common carriers of plastic flow and can be simultaneously activated when deforming a crystalline media [1–11]. An understanding of these mechanisms is not only relevant to a broad range of applications, e.g., metal forming, thermomechanical treatments of materials, shape memory alloy processing, elastocaloric applications, high-pressure physics, but also widely spread in nature, e.g., in geophysical processes.

Here, a focus is placed on materials in which the viscoplastic deformation can be conditioned by the interplay between all three deformation modes: dislocation motion, martensitic PTs, and twinning. In such scenarios, the coupling between these deformation modes will dictate the material microstructure evolution, such as PTs accompanied by the dislocation slip [12,13], and the PTs promoted by the dislocation-

* Corresponding author at: Department of Mechanical and Aerospace Engineering, NC State University, Raleigh NC 27695, USA.
E-mail addresses: vlevitas@iastate.edu (V.I. Levitas), lmxiong@iastate.edu (L. Xiong).

https://doi.org/10.1016/j.commatsci.2023.112508
Received 9 June 2023; Accepted 11 September 2023
Available online 26 September 2023

or twin-mediated plastic flow [8,14]. Several attempts on the study of the complex interaction between the dislocation-, twinning-, or PT-mediated plasticity include: (i) a simultaneous treatment of PTs, dislocations, and twinning within a continuum sharp interphase approach from the theoretical point of view in [15–17] and the numerical point of view in [18,19]; (ii) a smeared continuum description of the interaction of plasticity and PTs under high pressure; [20–22] (iii) continuum-level computational analysis of the effects of interfaces and twinning on the PTs through crystal plasticity finite element (CPFE) simulations, where twinning is found to promote the α to ω PTs but suppress the reverse PTs in zirconium [8]; (iv) phase field approach (PFA) consideration of discrete dislocations and PTs at the nanoscale in [23–27] and also at the microscale in [7,28]; and (v) atomistic simulations of interaction between PTs and plasticity in [3,29–31]. For a more comprehensive summary of the research progress in this field, a few representative review articles on this topic can be found in [32–35] and in [11,36–38] from the materials and mechanics point of view, respectively. It should be noted that, in the above literature, twinning in martensite is often considered as one part of the multi-variant martensitic PTs.

In this work, we aim to probe the mechanisms underlying the interaction between dislocation slip, PTs, reverse PTs, and twinning. A co-operation of these three deformation modes is pertinent to materials subjected to extreme mechanical environments (e.g., high pressure, high torsion, shock loads, etc.) [11,39–43]. Especially, the occurrence of dislocations and twinning may have a potential to decrease the critical pressure required for initiating PT. For example: (i) an irreversible PT from rhombohedral to superhard cubic boron nitride (BN) was obtained in [44] at 5.6 GPa under plastic straining but at 55 GPa under hydrostatic loading. A plastic strain-induced PT from hexagonal to superhard wurtzitic BN can be induced under a pressure as low as 6.7 GPa in a rotational diamond anvil cell (RDAC) while under hydrostatic loading it was not observed even at 52.8 GPa [45]; (ii) the plastic strain-induced PTs from graphite to hexagonal and cubic diamonds were observed in RDAC at 0.4 and 0.7 GPa, respectively, while under hydrostatic conditions they occurred at 20 GPa and 70 GPa, respectively [46]. Thus, the PT pressure reduction induced by a plastic straining may reach up to two orders of magnitude. Other than contributing to the PT pressure reduction, one more surprising effect is that the plastic straining under pressure may lead to new (hidden) phases that were not or could not be reached under hydrostatic conditions [11,39–42,47,48].

In order to understand the dislocation-PT interaction under high pressure, the fundamental difference between the plastic strain-induced PTs and the pressure- or stress-induced PTs was introduced [37,49]. In details, the stress-induced PT refers to the PT under stresses below the yield strength. It starts at the pre-existing defects. In contrast, the strain-induced PT occurs at the defects generated during the deformation. Particularly, the dislocation pileup at the grain boundaries (GBs) is considered as the strongest internal stress concentrator responsible for the strain-induced PT [37,49]. As stated above, the plastic strain-induced PTs can occur at pressures one to two orders of magnitude lower than that under hydrostatic conditions. It thus requires a completely different thermodynamic/kinetic description and experimental characterization. The analytical solutions in [37,49] derived from a model by treating the dislocation pileup as a super-dislocation shows that, because all the stress components at a pileup tip are proportional to the number of the dislocations in a pileup, the PT pressure can be reduced by a factor of 10 and more. This conclusion was elaborated within a nanoscale PFA of coupling the evolution of discrete dislocations with PTs in [25–27,50–52] and a microscale (or scale-free) PFA simulating the simultaneous shear (dislocation or twinning) and PT in a polycrystalline aggregate under compression and shear [7,28].

Despite their great success in providing explanation for the plastic strain-induced PT promotion, the above analytical treatments and nano-/micro-scale phase field simulations have a clear limitation: the GBs at which the dislocations pile up are modeled as fixed (with respect to material) lines, which cannot resolve the actual processes of interaction between dislocations and GBs. In order to capture more details about the slip-interface reaction and the subsequent structure changes, an atomistic resolution at the slip-interface intersection is necessary. Otherwise, the dislocation pileup's contribution to the subsequent PTs or twinning near the interface might be either under- or over-estimated. For example, our previous molecular dynamics (MD) simulations demonstrated that shuffle screw dislocations transmit through tilt GBs in silicon (Si) [53]. They simply cannot pile up and thus may not contribute much to a PT in Si. By contrast, 60° shuffle dislocations pile up at GBs and significantly promote the amorphization [54]. Also, quite often the dislocations are located in the high-pressure phase and pile up against an immobile PB, causing PT within the remaining low-pressure phase. Such a situation has not been resolved at the atomic level yet due to difficulties of avoiding the interface motion.

Clearly, it remains a challenge using single-scale techniques/methodologies to address the full complexity associated with the microscale dislocation pileup and the subsequent structure changes because: (a) a dislocation pileup may be tens of micrometer in length and introduce a high internal stress field spanning tens of microns away from the slip-interface intersection [55,56]; (b) the PT at the tip of a dislocation pileup compete with slip transmission, twinning [8,57–59], crack initiation [60–62], which all originate from the atomic scale and need to be resolved at a high resolution. Here we present a concurrent multiscale computational framework to address this challenge with a focus on understanding how a microscale dislocation pileup interacts with an atomically structured interface and how it contributes to the subsequent direct PTs, reverse PTs, and then twinning. It bridges the length scale gap between atomistic and continuum, and provides us with a platform for understanding the interactions between dislocation slip, PTs, and twinning from the bottom up.

2. Methodology

A concurrent atomistic–continuum (CAC) approach [63–76] built upon a formulation [77–83] that unifies the atomistic and continuum description of materials within one framework is deployed here. This formulation [80–83] is a generalization of the Irving–Kirkwood procedure [84–87] in statistical mechanics. It views the solid material as a collection of lattice cells continuously distributed in space, within each of which a group of discrete atoms is embedded. The continuum-level physical quantities, including mass density, linear momentum density, energy density, momentum flux (also referred as stress in continuum mechanics), and energy flux, are then defined in terms of the atomic positions, velocities, and interatomic forces through Dirac or Gaussian distribution functions [79,88]. An introduction of these physical quantities into the classical Newtonian mechanics leads to a series of equations, i.e., mass conservation, momentum balance, and energy conservation equations, which can govern the behavior of materials by considering them as a collection of atoms [80]. These equations are partial differential equations in the same form as the balance equations in classical continuum mechanics but with atomistic information being built-in. Thus, those equations can be solved using numerical techniques, such as finite-difference or finite element (FE), which are commonly used for solving the equations in continuum mechanics. The CAC simulation tool is an FE implementation [73,74] of this formulation.

Unlike the FE model in classical continuum mechanics, which considers the material as a collection of mass points without any internal structures, the material body in CAC is discretized into finite number of elements, each of which is a collection of the lattice cells with the atomistic information (crystal structure, slip planes, cleavage planes, interstitial sites, etc.) being embedded. Furnished with such atomistic information, comparing with the other concurrent multiscale models, CAC has several unique features: **(i)** it does not need additional constitutive rules and can be directly driven by the traditional interatomic potentials or the machine learning-based potentials to be trained from

ab initio calculation data; **(ii)** it does not need any special treatments to describe discontinuity, such as dislocations, PTs, or cracking, at the continuum level but with their atomistic nature being retained; **(iii)** it also does not need any sophisticated rules for passing the dislocation-mediated plastic flow from the atomistic domain to the continuum domain and vice versa [63–65]. At a fraction of the cost of full MD, CAC simulations have been performed to study: **(a)** the dislocation nucleation and growth in Cu, Al, Ni, and Si [66]; **(b)** the Si-I → Si-II PT in Si [74]; and **(c)** the dislocation transmission across a twin boundary (TB) in bi-crystalline metals [65]. It has a predictive capability at approximately the same level as that of MD but demands significantly less computational resources. This thus provides us with an ideal platform for understanding the interplay between the microscale dislocation slip and the subsequent PTs/twinning nearby an atomically structured interface.

Here, as a first demonstration of its applicability in solving such problems, a two-dimensional (2D) two-phase material (the hexagonal and square phases co-exist with an incoherent interface in between) under compression and shear is selected as a model system because: **(i)** the 2D set-up enables a direct comparison of the simulation results with the analytical solutions under plane strain conditions for validation purpose; **(ii)** if desired, the interface structure in such systems can be manipulated to model the interfaces in a few recently developed high-performance metallic composites, such as Ti/Al [89], Mg/Nb [90], Cu/Nb [91], and among several others. **(iii)** the dislocation-induced local stresses in many realistic 2D materials (crystalline solids consisting of a single layer of atoms), such as one single layer of graphene sheet, boron nitride [92–95], or colloidal crystals [96,97], may have significantly contributed to the PTs in them but has not been fully understood yet.

The rest of this paper is structured as follows. In Section 3, we briefly introduce the interatomic potential, the crystal structure, the PT variants, the boundary conditions, and also the loading strategies. The atomistic together with the multiscale computational analysis on the dislocation pileup formation process, the pileup-induced stress accumulation, as well as its role in the subsequent PTs, reverse PTs, and twinning are then presented in Section 4. Thereafter, we conclude this paper with a summary of our major findings as well as a brief discussion of future research in Section 5.

3. Simulation details

3.1. Interatomic potential and PT variants

For the chosen material system, the atomic interaction in both square and hexagonal lattices is described using a modified Lennard–Jones (L–J) potential by Lee [98] as shown in Eq. (1):

$$V_{MLJ} = -4\epsilon[(\frac{\sigma}{r})^6 - (\frac{\sigma}{r})^{12}] - \frac{H}{\sigma_h\sqrt{2\pi}} e^{[-\frac{(r-r_{mh})^2}{2\sigma_h^2}]}, \quad (1)$$

which was originally proposed to study the bcc-to-hcp PT in iron. The modified functional form of the L–J potential in Eq. (1) is the combination of a traditional L–J (12–6) term and an inverse Gaussian term. The 12–6 term leads to a stable hexagonal crystal structure at zero stress. The addition of an inverse Gaussian into the L–J potential gives rise to a square lattice. To satisfy the needs of simultaneously modeling dislocations, PTs, and their interactions in square-hexagonal lattice composites, here we start with the well-established L–J model parameters for fcc solids together with a set of initially guessed values for H, r_{mh}, and σ_h in Eq. (1). Then, an iterative procedure is utilized to modify those initial guesses to stabilize: **(i)** an incoherent interface between the square and the hexagonal phase, which acts as an obstacle to the dislocation motion; and **(ii)** the core structure of a dislocation in the hexagonal phase. The parameters satisfying these two conditions are listed in Table 1.

Table 1
The parameters of the modified L-J potential for the square and the hexagonal phases.

mass (g/mole)	σ (Å)	ϵ (eV)	H (eV Å)	r_{mh} (Å)	σ_h (Å)	cut-off (Å)
63.546	2.277	0.415	−0.4964	3.6432	0.4772	5.0094

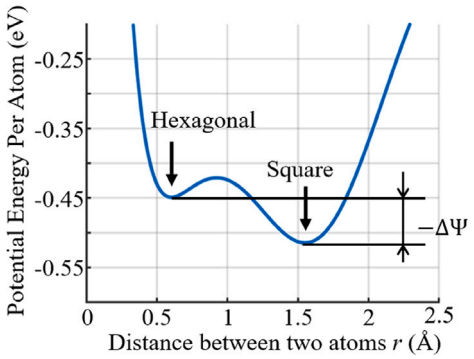

Fig. 1. The potential energy per atom in the material system under consideration here is described by a modified Lennard–Jones potential in Eq. (1).

In the absence of chemical heterogeneity, the atomic structure of materials with certain crystallographic configuration, such as fcc, bcc, hcp, diamond, zinc blend, and so on, can be determined by one single parameter: the potential energy per atom. The calculation of the potential energy as a function of the interatomic separation, i.e., the $E - r$ relation, is often used to provide researchers with important information, such as: (i) the r at which E becomes minimal is the equilibrium distance, r_0, between atoms in the ground state; (ii) the pressure-induced PT from one phase to another phase occurs along the common tangent line of the $E - r$ curves of those two phases. According to the potential energy functional form in Eq. (1) and its parameters in Table 1, the calculated $E - r$ curve is presented in Fig. 1. Three key observations from Fig. 1 are: (1) this potential energy landscape has a minima at 0.595 Å and 1.525 Å for the hexagonal and square phases, respectively; (2) the square phase should be the ground state because it has a lower potential energy minimum than that of the hexagonal phase; and (3) the potential energy difference between hexagonal and square phases under zero stress is $\Delta\Psi = 0.066$ eV. Although the square-to-hexagonal PT occurs under non-zero stresses, our simulations confirm that the hexagonal phase itself is metastable and can exist under zero stress. In this way, the chosen potential indeed enables us to stabilize two different lattices within one model. With a deployment of this potential, the unit cell configurations of the hexagonal and square phases under consideration here together with the transformation deformation gradient between those two phases can be found in Appendix A.

3.2. The computer model setup

In order to determine the role of a dislocation pileup in the subsequent structure changes near the interface, the CAC model for a two-phase material system with square and hexagonal lattices co-existing is constructed (Fig. 2a). Clearly, when this system is subjected to loading, the deformation behavior near the square/hexagonal interface is critical and may dictate the material's overall microstructure evolution. The material domain near the interface is thus resolved at a fully atomistic resolution (Fig. 2b). In contrast, away from the interface, a CG description of the hexagonal phase using FE is deployed (Fig. 2b), which has much less degrees of freedom (DOF) than that of a fully atomistic model. The periodic boundary condition (PBC) is applied along the sample thickness direction. In this way, the dislocations, which are initially built in the model can be considered as the line

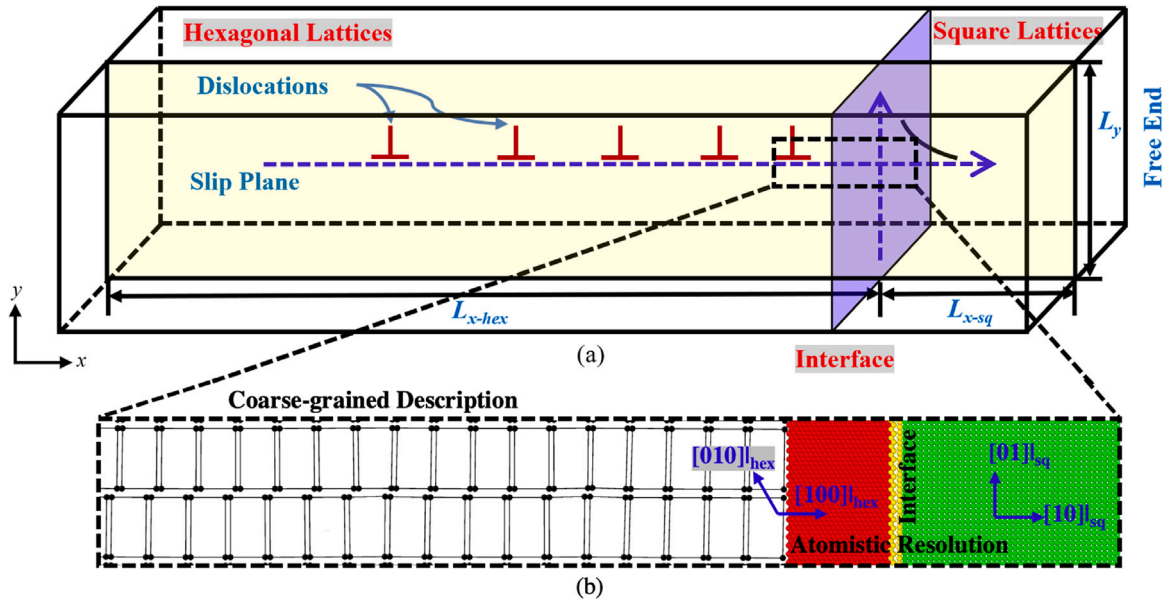

Fig. 2. The CAC model setup for simulating a dislocation slip-interface interaction in a 2D two-phase material: (a) the CG description of dislocations in the hexagonal phases away from the interface and the atomistic resolution near the interface; and (b) a zoom-in display of the FE and the atomic configuration in the dashed box of (a).

defects with an infinite length. Correspondingly, this square-hexagonal interface can be then considered as a plane defect. The sketch in Fig. 2 presents the such a model set-up in a 3D view, although the simulations in this work are actually performed in a two-dimensional space. To study the slip-interface reaction, similar to our previous work [63–65], the FEs are carefully aligned with their boundaries being along the dislocation slip planes in the hexagonal lattice. Each FE contains sixty-four atoms and can slide with each other along the element boundaries, which are shown as the vertical and horizontal lines in Fig. 2b. In this way, the dislocation-mediated slip far away from the interface can be accommodated in the CG domain. More importantly, since each FE in Fig. 2b is a collection of lattice cells, the forces acting on the FE nodes are calculated by converting the interatomic forces into the internal force density using a Gauss quadrature scheme elucidated in [73,74]. As such, the constitutive rule for the atomistic and CG domains in the CAC model is the same, i.e., the interatomic potential in Eq. (1). This differs from other continuum approaches which accommodate dislocations through the deployment of either a contact model in [7,28], a Heaviside step function in [99], or an additional DOF in CPFE [100,101].

Here we have carefully chosen the crystallographic orientation of both the hexagonal and square lattices to construct the incoherent interface (Fig. 2b) such that: **(a)** the initially introduced dislocation slip is perpendicular to the interface, and **(b)** a dislocation transmission across the interface is suppressed, which has been justified through a detailed Schmid factor analysis and geometric compatibility factor analysis in [102]. In this way, a large number of dislocations can be piled up at the interface. A high internal stress is then generated ahead of the slip-interface intersection. Their contributions to the subsequent PTs can be in turn, well quantified without the need of considering transmission, cross-slip, and among several other complexities. Although the interface here satisfying the above two conditions may not be the one with an energy minimum, in practice, the majority of interfaces found in materials will not be at a minimum energy state anyway due to the presence of defects.

A queue of dislocations with a uniform separation of 12 nm in between are initially introduced into the hexagonal lattice, which is now in a CG description (Fig. 2b) similar to that has been used in our previous work [63–65]. An introduction of each dislocation into the CG domain is realized here through displacing FE nodes according to the analytical solution for the displacement field around an edge dislocation derived from the theory of elasticity. Different from traditional FE models in which the neighboring elements are connected by sharing the FE nodes, the FEs in CAC models across the slip plane are disconnected (See Fig. 2b). Thus, the displacement jump induced by a dislocation along the slip plane will be allowed. It should be also noted that the dislocation displacement fields, strain and stresses resulting from present CAC simulations will deviate from the linear isotropic elasticity-based solution. Instead, the actual atomic-level information, including crystal anisotropy, finite strain, nonlinear elasticity, and the interface structure heterogeneity will be all considered. The reason that we initially introduce dislocations through displacing the FE nodes according to the elasticity-based solution is to accelerate the convergence of our calculations by reducing the time required for equilibrating the system. For the model size under consideration in this work, we find that, when more than 18 dislocations are initially built into the sample, several dislocations nearby the interface will cross slip. To eliminate the cross slip-induced complexity, only 16 dislocations are initially built into the model. Similarly, for the nano-sized MD models to be used for verifying CAC simulation results, only eight dislocations are included. The left and right ends of the sample along x direction are free. A homogeneous shear within the xy plane is imposed until a desired shear stress is achieved. Thereafter, the top and bottom ends of the sample along y direction are fixed for equilibrating the dislocation configuration in the pileup. When a PT needs to be activated, a displacement controlled compressive loading along y direction will be then applied on the two ends of the sample.

Due to the deployment of a CG description in the region away from the interface, the hexagonal lattice dimension, noted as $L_{x-\mathrm{hex}}$ in Fig. 2a, in the CAC model can be at the micrometer level. It enables us to initially introduce tens of dislocations into the model. This goes beyond the reach of a traditional MD model because MD usually has a limited length scale at nanometers, which can only accommodate a few dislocations in the pileup [103]. On the other side of interface ahead of the pileup tip, the crystal structure is in a square lattice with a dimension of $L_{x-\mathrm{sq}}$ along x direction. The sample dimension along y direction is chosen as $L_y = m_{\mathrm{hex}} a_{\mathrm{hex}} = n_{\mathrm{sq}} a_{\mathrm{sq}}$, where m_{hex} and n_{sq} are the numbers of the hexagonal and square lattice cells along y direction, respectively. In addition to microscale CAC models, a series of nanoscale MD simulations are also performed using LAMMPS [104]. In all these simulations, the displacement along z direction

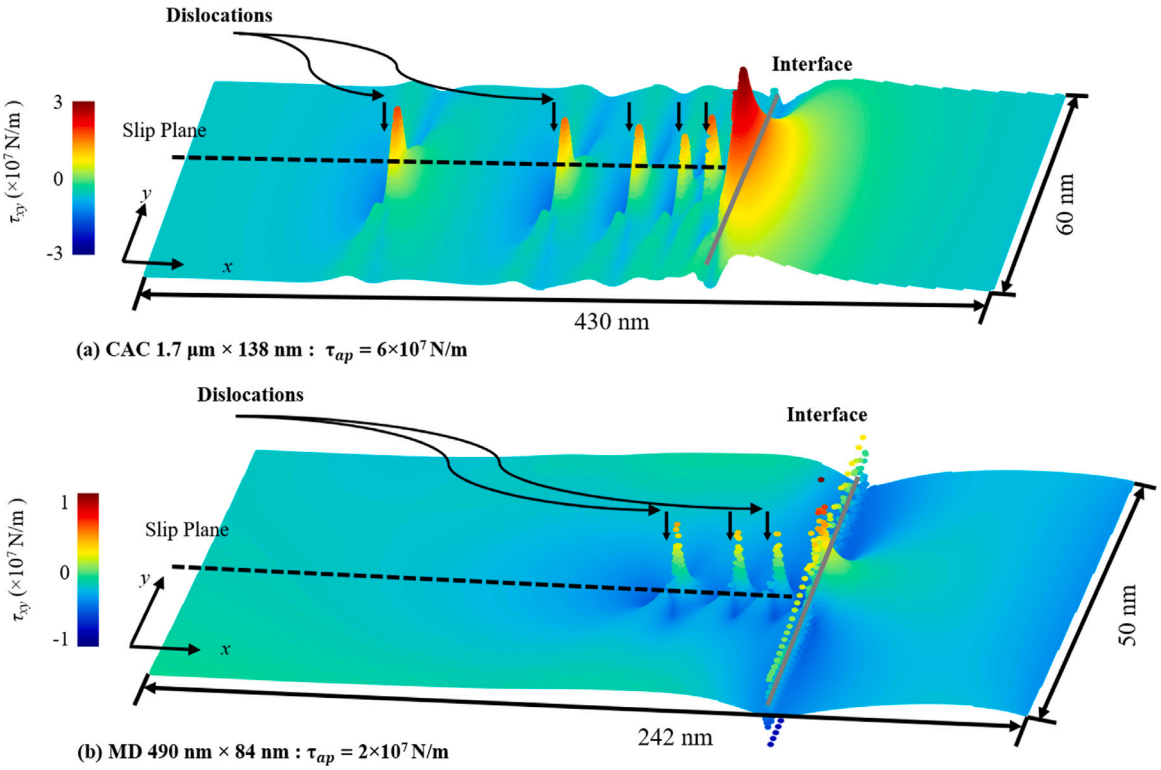

Fig. 3. The dislocation pileup configuration and the contour of the internal stresses (the applied stress, τ_{ap}, is not included here) from (a) microscale CAC: 16 dislocations are piled up against the interface under a shear $\tau_{ap} = 6 \times 10^7$ N/m; 6 of them arrive at the interface; (b) nanoscale MD: 8 dislocations are piled up at $\tau_{ap} = 2 \times 10^7$ N/m; 5 of them arrive at the interface.

Table 2
The dimensions and the number of the DOF in MD and CAC models.

	$L_{x-\text{hex}}$	$L_{x-\text{sq}}$	L_y	DOF	Number of dislocations in a pileup
Microscale CAC	1.58 μm	120 nm	138 nm	315,528 FE nodes + 118,392 atoms	16
Nanoscale CAC	420 nm	70 nm	84 nm	55,416 FE nodes + 20,982 atom	8
Nanoscale MD	420 nm	70 nm	84 nm	1,355,284 atoms	8

(thickness direction) of the sample is constrained to achieve a plane strain condition. The initial crystallographic orientations of square and hexagonal lattices are indicated in Fig. 2b. The dimensions and the number of the degree-of-freedom (DOF) in both nanoscale MD and microscale CAC models are listed in Table 2.

3.3. Dislocation pileup process

The computational models containing the built-in dislocations are firstly relaxed for a duration of 20 ps with a time step of 1 fs to achieve a stable configuration. Thereafter, a shear stress, noted as τ_{ap}, is imposed on the whole samples to drive the dislocations towards the interface. A certain level of τ_{ap} is realized through applying a homogeneous shear strain while monitoring the resulting shear stress on the fly. If the shear stress does not match the desired τ_{ap}, the shear stress is adjusted by increasing or decreasing the applied shear strain. When τ_{ap} arrives at the desired value, the top and bottom boundaries of the sample are constrained and not allowed to move along both x and y directions any more.

An internal stress concentration, noted as τ_{xy}, ahead of the slip-interface intersection is generated due to the large number of dislocations' arrival at the interface. Figs. 3a and 3b show the contour of the internal stress field obtained from CAC and MD simulations of 16 and 8 dislocations piling up at the interface under a shear of $\tau_{ap} = 6\times10^7$ N/m and $\tau_{ap} = 2\times10^7$ N/m, respectively. It should be noted that the contour here shows the magnitude of $\tau_{xy} - \tau_{ap}$, rather than the absolute value of τ_{xy}. It is seen that the level of the internal stress concentration ahead of a pileup tip in Fig. 3a is significantly higher than that in Figue 3b, because more dislocations have participated in the formation of a pileup in CAC (Fig. 3a) than that in MD (Fig. 3b). The detailed analysis of the dislocation pileup-induced internal stress profiles and their fitting into the classical Eshelby model, the super-dislocation model, as well as a combination of the Eshelby and the super-dislocation model can be found in Appendix B.

With an atomistic resolution at the interface, CAC provides us with an opportunity of examining the atomic-level structure evolution at the slip-interface intersection. Fig. 4 presents the snapshots showing the atomic structure configuration (red: square lattice; blue: hexagonal lattice; green: defects) when different number of dislocations arrive at the interface. It is seen that, when τ_{ap} is at a level of 1.3×10^7 N/m, one dislocation is behind the pileup tip and two dislocations arrive at the interface, a step with a height of 5.12 Å, i.e., the magnitude of two Burgers vector, $2\boldsymbol{b}$, is formed (Fig. 4a). This step can be approximately considered as a single super-dislocation with a Burgers vector of $N_a\boldsymbol{b}$, where N_a is the number of the dislocations arriving at the interface. Upon a further increase up to $\tau_{ap} = 7.1 \times 10^7$ N/m, 9 dislocations arrive at the interface and eventually, leading to the formation of a step with a height of $9b$ (Fig. 4b). Under a shear stress of $\tau_{ap} = 10.6 \times 10^7$ N/m, 15 dislocations arrive at the interface, Fig. 4c show the corresponding atomic arrangements. At this stage, approximately, the step at the interface has a height of $15b$.

As designed, the interface under consideration here indeed blocks the motion of dislocations without allowing any transmission. Also, as

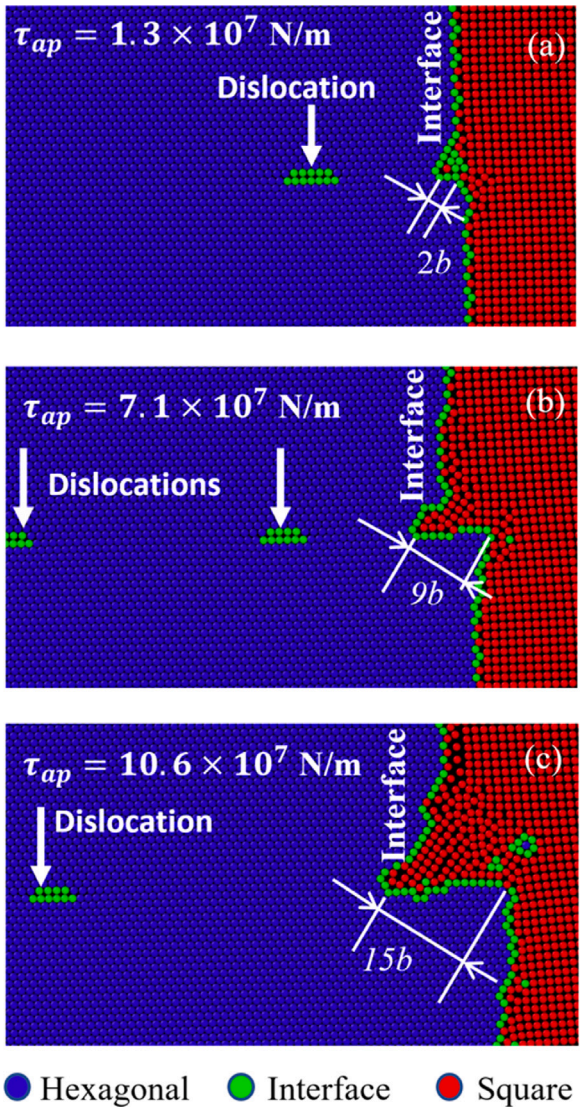

Fig. 4. The atomic-scale structure evolution at the slip-interface intersection when different number of dislocations arrive at the interface under different applied stresses, τ_{ap}. The atoms are color coded through an atomic-level coordination number analysis. The step formation at the slip-interface intersection is similar to a super-dislocation acting as a strong stress concentrator.

shown in [102], the dislocation configuration behind the pileup tip in Fig. 3 actually matches an analytical solution from Hirth and Lothe very well. More importantly, the step-like super-dislocation with a complex local structure is formed at the slip-interface intersection. Due to the local atomic structure reconstruction, this super-dislocation carries a sophisticated core structure rather than a simple additive of multiple dislocation cores. Similar features were observed in our previous full MD simulations of dislocation pileup against a tilt grain boundary in silicon, in which the amorphization has been found ahead of a slip-interface intersection [54]. It should be also noted that the presence of a thermal bath would likely promote the re-arrangement of the atoms at the interface and may promote a dislocation transmission. Without including any thermal fluctuations, the present simulations should be considered as extreme cases for the slip-interface reaction. A resolution of the thermal-induced atomic structure reconfiguration during the slip-interface reaction at finite temperature is beyond the scope here and will be studied in our future work.

4. Simulation results

4.1. Pileup-assisted PTs and twinning

4.1.1. The two-variant hexagonal phase formation

Through a displacement-controlled boundary condition, the pre-sheared sample is compressed along y direction. During the compression, the pre-shear τ_{ap} is maintained. Under the applied pre-shear τ_{ap}, the top and bottom boundary layers of the sample are then held as rigid and forced to move towards each other at 0.2 m/s. This allows us to determine the role of a dislocation pileup in the subsequent structure changes, such as PTs, reverse PTs, and twinning, if there would be any.

Firstly, the dislocation pileup-induced strain localization together with the local atomic structure changes are analyzed by calculating the atomic-level deformation gradient tensor, $\boldsymbol{F}$, the Lagrangian strain tensor $\boldsymbol{E} = 1/2(\boldsymbol{F}^T \cdot \boldsymbol{F} - \boldsymbol{I})$, and also the coordination number using OVITO [105]. The time sequences of the snapshots showing the atomic structure evolution during the PT process from CAC simulation (7 dislocations have arrived at the interface and another 9 of them are behind the pileup tip) are displayed in Fig. 5. The atoms in the first row of Fig. 5 are colored in a shear strain component of E_{xy} and the atoms in the second row are colored according to their coordination number with a cutoff of 3.92 Å. The coordination number analysis in Fig. 5 clearly shows that, at an early stage of the compression (from t = 12 ps to t = 15 ps), there exists a direct PT, i.e., from square (red) to hexagonal (blue), ahead of the dislocation pileup tip. During such direct PTs (square-to-hexagonal), the PT occurs through simultaneously activating two variants of the hexagonal phase as shown in Fig. 5. When these two transformed domains are in contact with each other, a twin boundary (TB) is formed. In details, at t = 12 ps, two atomic layers ahead of the pileup tip in the square phase are sheared to form a stacking fault, a precursor of the hexagonal phase. With a further increase of the loading, the stacking faulted atomic layers transforms to the hexagonal phase at t = 14 ps. The shear strain associated with the newly formed hexagonal phase above the slip plane is in an opposite sign (blue) comparing with that (orange) below this plane (see the first row of Fig. 5 from t = 14 ps and t = 17 ps). This corresponds to the two variants in the newly formed hexagonal phases, which are twinned with respect to each other and separated by a TB in between. Upon a further increase of the loading, the newly formed hexagonal phase grows into a wedge shape. The interface between the product (hexagonal) and the parent (square) phases contains many steps, avoiding the high-energy irrational interfaces. As a cross validation, the CAC simulation-predicted microstructure evolution during such a dislocation pileup-induced PTs is also directly compared with that from full MD simulations in Appendix C.

4.1.2. Twinning in square phase via a reverse PT

Interestingly, at a later stage of the deformation, the coordination number analysis in the second row of Fig. 5 when t = 15 ps and t = 17 ps shows that, at the slip-interface intersection, the newly formed hexagonal phases ahead of the pileup tip transform back to the square phases. This is referred as a reverse PT, i.e., hexagonal-to-square PT. The finish of the square-to-hexagonal PT and then the onset of a reverse PT are believed to be caused by the atomic structure reconfiguration at the slip-interface intersection, which has largely released the local internal stresses. The newly formed square phase resulting from such a reverse PT together with the original square phases form a twinned structure. Although the twinning formation through a direct PT was reported in literature [106–109], our finding here is believed to be the first demonstration of twinning formation during a monotonous loading through a dislocation pileup-induced PT and then a reverse PT. In other words, twinning does not occur directly in the square phase, but occurs via a direct-to-reverse PT instead. Analytically, when the elastic strains

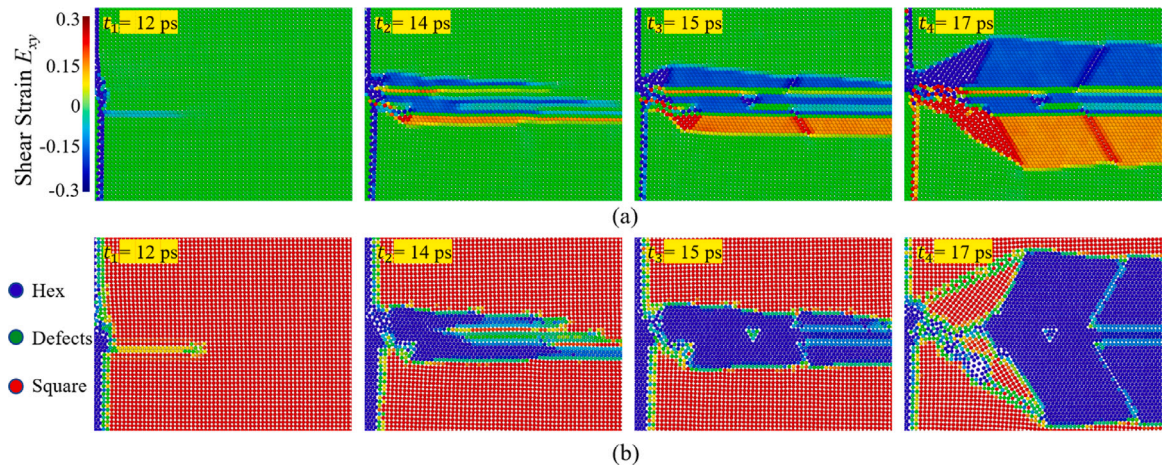

Fig. 5. The time sequences of the atomic-scale structure evolution ahead of the pileup tip in CAC simulations showing the process of a square-to-hexagonal PT (direct) and then the hexagonal-to-square PT (reverse) in pre-sheared two-phase materials under compression. The atoms in the first row of this figure are colored in a shear strain of E_{xy} and the second row is colored according to their coordination number with a cutoff of 3.92 Å.

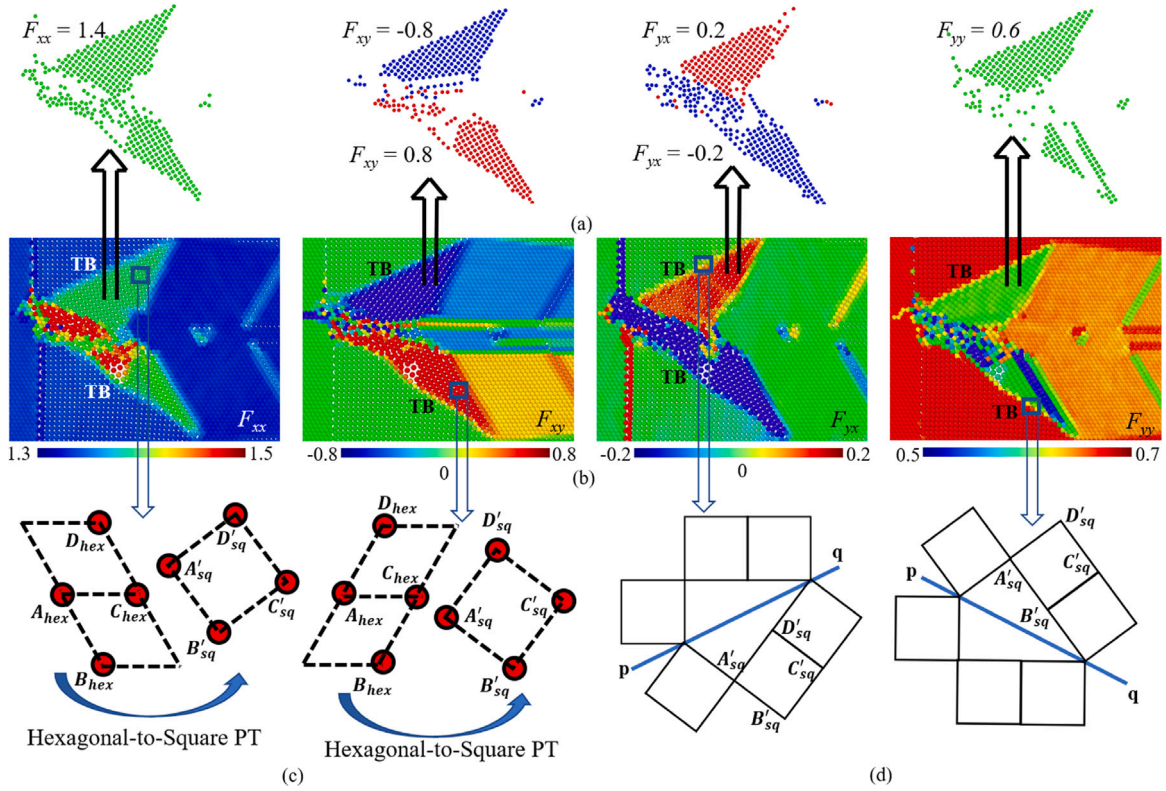

Fig. 6. (a) The atomic configuration in the square phase resulting from the hexagonal-to-square PT (reverse PT). Here the atoms are colored in their deformation gradient components, F_{xx}, F_{xy}, F_{yx}, and F_{yy}, respectively. Only the atoms with $F_{xx} = 1.4$, $F_{xy} = 0.8$, $F_{yx} = 0.2$; and $F_{yy} = 0.6$ are displayed; (b) One snapshot at $t = 17$ ps showing the atomic configuration ahead of the pileup tip in CAC simulations with all the atoms being displayed and colored in F_{xx}, F_{xy}, F_{yx}, and F_{yy}, respectively; (c) an atomic-scale sketch showing how the two variants in the hexagonal phases transform back to the square phase; and (d) a sketch elucidating the formation of the twinned structure in the square phases with a TB (noted as ***pq***) in between the original square phases and the newly formed square phase resulting from the reverse PT.

are neglected, the transformation deformation gradients, $\boldsymbol{U}_i$ and $\boldsymbol{U}_j$, in the two regions across a twin boundary (TB) satisfy

$$\boldsymbol{Q}_i \cdot \boldsymbol{U}_{ti} - \boldsymbol{Q}_j \cdot \boldsymbol{U}_{tj} = \gamma_t \boldsymbol{m}\boldsymbol{n}. \tag{2}$$

, where γ_t is the twinning shear, $\boldsymbol{m}$ is the twinning direction within the twinning plane which has a unit normal of $\boldsymbol{n}$. Eq. (2) is used here to check whether the newly formed square phase resulting from the reverse PT is indeed twinned with respect to the original square phase. For the observed reverse PT, i represents an original square phase, and j is for the domain in which the material is in a square phase resulting from the hexagonal-to-square PT. Then $\boldsymbol{Q}_i = \boldsymbol{U}_i = \boldsymbol{U}_j = \boldsymbol{I}$, and Eq. (2) is simplified as

$$\boldsymbol{I} - \boldsymbol{Q} = \gamma_t \boldsymbol{m}\boldsymbol{n}, \tag{3}$$

which has at least two solutions as following:

$$\gamma^+ = 0.25; \quad \boldsymbol{m}^+ = \{4/\sqrt{5}, 2/\sqrt{5}\}^T;$$
$$\boldsymbol{n}^+ = \{2/\sqrt{5}, -4/\sqrt{5}\}; \quad \boldsymbol{Q}^+ = \begin{pmatrix} 1.4 & -0.8 \\ 0.2 & 0.6 \end{pmatrix}; \tag{4}$$

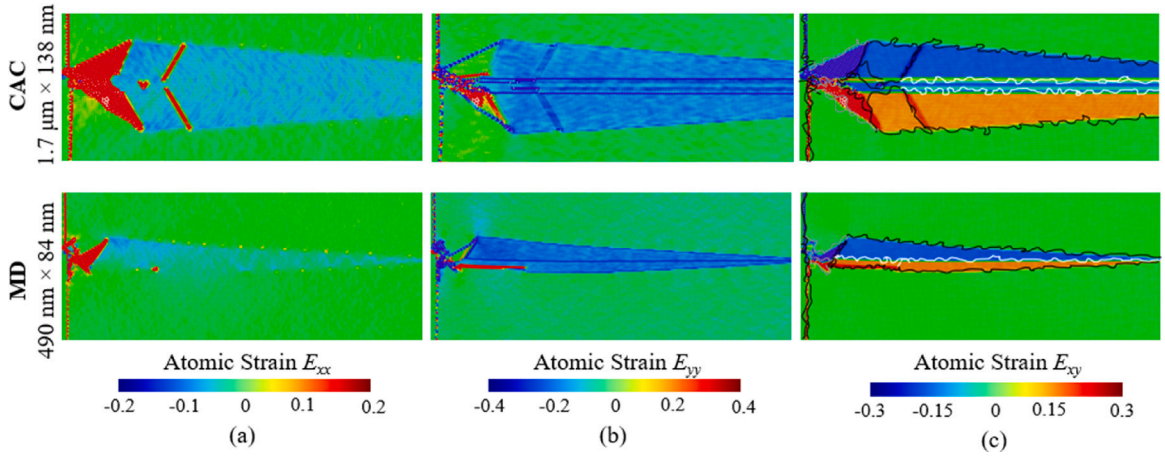

Fig. 7. The contour of the atomic-level strain at $t = 17$ ps: (a) E_{xx}; (b) E_{yy}; and (c) E_{xy} showing the simultaneous occurrence of twinning and PTs ahead of the dislocation pileup from CAC and MD simulations. This solution corresponds to the stationary state. The black lines correspond to the phase interface equilibrium condition of $X = 0$ with deformation gradients being taken from the parent and product phases, while the white lines correspond to the twin interface in an equilibrium condition of $X = 0$ with the deformation gradients being taken from the twinning variants across the TB.

or

$$\gamma^- = 0.25; \qquad \boldsymbol{m}^- = \{4/\sqrt{5}, -2/\sqrt{5}\}^T;$$
$$\boldsymbol{n}^- = \{2/\sqrt{5}, 4/\sqrt{5}\}; \qquad \boldsymbol{Q}^- = \begin{pmatrix} 1.4 & 0.8 \\ -0.2 & 0.6 \end{pmatrix}. \tag{5}$$

To compare our simulation results against the above analytical solutions, the atomic-level deformation gradient components, F_{xx}, F_{xy}, F_{yx}, and F_{yy}, from CAC simulations at t=17 ps are calculated using the initially undeformed atomic configuration as a reference and shown in Fig. 6a. It is seen that the simulation-based $\boldsymbol{F}$ in the region where the reverse PT occurs agrees with the analytical solution of $\boldsymbol{Q}$ very well. Therefore, the square phase resulting from such a reverse PT is indeed twinned with respect to the original square phase. In more details, for the region where the reverse PT occurs, the atomic configuration at the dislocation pileup tip is shown in Fig. 6b. Here all the atoms are displayed and colored by their deformation gradient, F_{xx}, F_{xy}, F_{yx}, and F_{yy}, respectively. Based on the detailed crystallographic orientation analysis (Fig. 6c), the TB formation process is also sketched in Fig. 6d for clarifications.

4.1.3. Thermodynamic driving force at the interfaces

In addition to the atomic-level deformation gradient tensor as shown in Fig. 6, for the snapshot at $t = 17$ ps in Fig. 5, three components of the Lagrange strain tensor, E_{xx}, E_{yy} and E_{xy}, associated with each atom ahead of the slip-interface intersection are also extracted and presented in Fig. 7. In order to quantify how the local stress contributes to the subsequent PTs, an atomic-level local strain together with a local stress-based thermodynamic driving force analysis (similar to that for nanoscale [51,52] and scale-free [7,28,110] PFAs) are also performed here. Based on the atomic-level local stresses, the thermodynamic Eshelby-type driving force for PT and twinning, X is defined as:

$$X = \boldsymbol{P}^T : (\boldsymbol{F}_{t2} - \boldsymbol{F}_{t1}) - \Delta\Psi. \tag{6}$$

Here, $\boldsymbol{P} = J\boldsymbol{\sigma} \cdot \boldsymbol{F}^{-1T}$ is the first Piola–Kirchhoff stress expressed in terms of the Cauchy stress $\boldsymbol{\sigma}$ with $J = det\boldsymbol{F}$. $\Delta\Psi$ is potential energy difference between the stress-free phases from both sides of each interface (which is zero for twin boundaries). $\boldsymbol{F}_{t1}$ and $\boldsymbol{F}_{t2}$ are the transformation deformation gradients in the two material domains across an interface. In particular, for the TBs in the hexagonal phases, they are $\boldsymbol{F}_t^+$ and $\boldsymbol{F}_t^-$ in Eq. (A.1), respectively. For the TBs in the square phases ahead of the pileup tip, they are $\boldsymbol{I}$ and $\boldsymbol{Q}^+$ or $\boldsymbol{Q}^+$ in Eqs. (4) and (5). For the PBs between hexagonal and square phases, they are either $\boldsymbol{F}_t^+$ or $\boldsymbol{F}_t^-$ and the transformation deformation gradient in the square phase, $\boldsymbol{I}$, $\boldsymbol{Q}^+$ or $\boldsymbol{Q}^-$, respectively. The condition of $X = 0$ corresponds to the local thermodynamic equilibrium of the relevant interface under consideration.

The black lines in Fig. 7c correspond to the phase interface equilibrium condition of $X = 0$ with the deformation gradients in it being taken from the parent and product phases across the interface. By contrast, the white lines correspond to the twin interface equilibrium condition of $X = 0$ with the deformation gradients in it being taken from the two twinning variants across the TB. Fig. 7c shows that, during the processes of direct PTs, reverse PTs, and twinning, all interfaces (including initial vertical phase interface) correspond to the continuum phase equilibrium condition of $X = 0$. Thus, these interfaces are stationary. Although this has been shown for cubic-tetragonal phase interface in nanoscale [51,52] and scale-free [7,28,110] PFAs at the continuum level, it is observed for the first time here at the atomic scale with a variety of different twinning interfaces being included.

4.2. The role of the pileup-induced local stresses in the subsequent PTs

In order to quantify how the dislocation pileup-induced local stresses contribute to the subsequent PT, we perform a series of analysis on how the square phase responds to compression through plotting the (σ_y- ε_y) curves (Figs. 8a–b). Here, ε_y is the Lagrangian strain along y-direction. The stress, σ_y, is an average of the true stresses along y-direction acting on the atoms located in a domain (100 nm × 22 nm in CAC and 60 nm × 15 nm in MD, respectively) ahead of the dislocation pileup tip. Results in Figs. 8a–b show that: **(i)** prior to $\varepsilon_y = 0.02$, both CAC and MD simulations predict a linear stress–strain relation with the same modulus of E. At larger strains, the material behavior is highly nonlinear though; **(ii)** thereafter, a plateau appears on all the stress–strain curves; **(iii)** a square-to-hexagonal PT is found to start at ε_y where the plateau appears. This corresponds well to the atomic configuration evolution in Figs. C.1 and C.2; **(iv)** the critical compressive stress required for the occurrence of PT can be thus identified as σ_c in Figs. 8a–b; and **(v)** σ_c largely decreases when the pre-applied shear is increased from $\tau_{ap} = 2\times10^7$ N/m to $\tau_{ap} = 8\times10^7$ N/m. The considerable reduction of σ_c with the increase of τ_{ap}, i.e., from $\sigma_c = 16\times10^7$ N/m at $\tau_{ap} = 2\times10^7$ N/m to $\sigma_c = 4\times10^7$ N/m at $\tau_{ap} = 8\times10^7$ N/m, can be attributed to the large number of dislocations accumulated at the interface, which has introduced a high local stress assisting the PT at the pileup tip.

Furthermore, Fig. 9 presents the data from both CAC and MD simulations for quantitatively relating the critical stress, σ_c, at which the PT starts, with the previously determined stress intensity factor K_b (the stress intensity factor induced by the dislocations behind the pileup

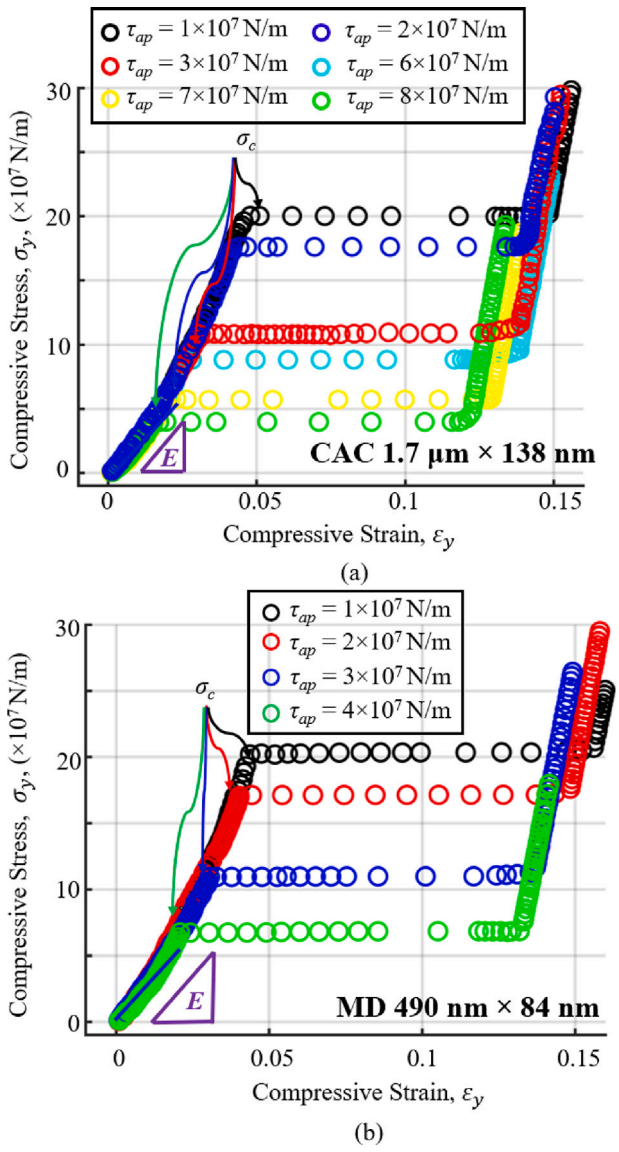

Fig. 8. The stress–strain curves from (a) CAC and (b) MD simulations of PTs in multi-phase lattices under compression after the pileup of a certain number of dislocations at the interface under different τ_{ap}.

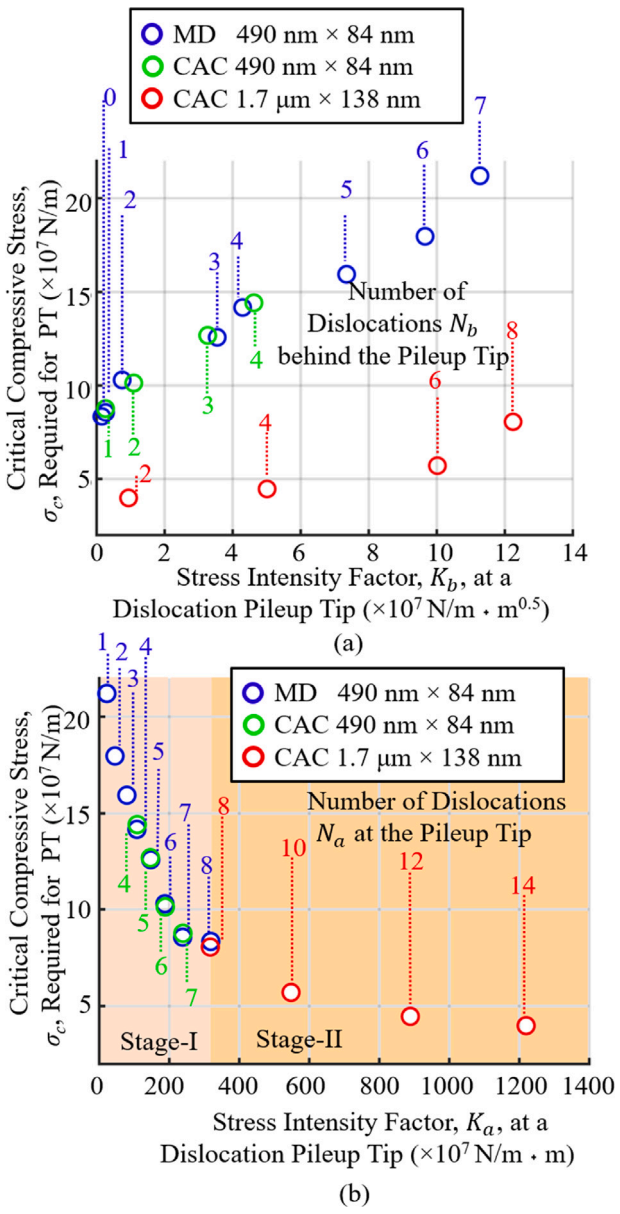

Fig. 9. The relationship between the stress intensity factors (a) K_b behind the pileup tip, (b) K_a ahead of the pileup tip and the critical compressive stress σ_c required for activating the PT in both the nanoscale MD and microscale CAC simulations.

tip) and K_a (the stress intensity factor induced by the dislocations at the pileup tip). Detailed calculation of K_a and K_b can be found in Appendix B). Fig. 9 clearly shows: **(i)** the σ_c required for initiating the PTs can be as high as 22×10^7 N/m if only one dislocation has been initially introduced into the model, but can be reduced to 4×10^7 N/m when 16 dislocations are piled up at the interface. This corresponds to PT pressure reduction by a factor of 5.5; and **(ii)** the relation between σ_c and the internal stress intensity factor, K_a and K_b, can be divided into to two stages . Upon an increase of K_b and K_a, σ_c in Stage-I reduces considerably faster than it does in Stage-II.

The above results suggest that, for the material system under consideration here, the stress, σ_y, applied along y direction, is not the only stress component that contributes to the PT. Eq. (6) allows us to analyze all the stress components' contributions to the PT driving force, X, in materials corresponding to different transformation strain components. The larger the transformation reduction in volume is, the larger the effect of the hydrostatic pressure is. The more pronounced the transformation shear is, the stronger the influence of the shear stresses. In the present computational set-up, at the slip-interface intersection, there is only a notable concentration of shear stress, σ_{xy}; the normal stresses, σ_x, σ_y, as well as the hydrostatic pressure, $-0.5\,(\sigma_x+\sigma_y)$, are all orders of magnitudes lower than σ_{xy}. That is why the main contrition to the driving force, X, is produced by shear stresses, and normal components of the $(\boldsymbol{F}_{t2}-\boldsymbol{F}_{t1})$, as well as jump in volume are not important. However, away from the interface, where the concentration of shear stresses due to the dislocation pileup decays, the effect of normal stresses and components of $(\boldsymbol{F}_{t2}-\boldsymbol{F}_{t1})$ is getting more pronounced.

5. Concluding remarks

To summarize, here we present an atomistic-to-microscale computational analysis of the interplay between dislocation slip and PT/twinning in two-phase materials under compression and shear. One main novelty of the CAC approach deployed here is its capability in bridging the relevant length scales by resolving the structure changes near an interface at the atomic scale while the lagging dislocations

away from the interface in a coarse-grained atomistic description. It thus expands the MD-simulation-based predictive capability from the nanoscale to the micrometer level. The main findings of this study are summarized as below:

(1) The micron-sized CAC model can accommodate tens of dislocations at a modest computational cost. These dislocations may be blocked by the obstacles (an incoherent interface in this work) and form a pileup spanning a range of several micrometers (1.2 μm in the present model). By contrast, the nanoscale MD model using the same computational resource can only accommodate up to 8 dislocations in a pileup, the equilibrium configuration of which under certain shear stress only spans tens of nanometers;

(2) A high internal stress concentration appears ahead of the tip of a pileup containing a large number of dislocation, which surprisingly follows neither the classical Eshelby model (assuming the interface as a rigid obstacle to dislocations) nor the super-dislocation model (assuming the formation of a perfect step at the interface upon the arrival of all the dislocation) but a combination of them (Eq. (B.1));

(3) The dislocation pileup-induced internal stress intensity factor is linearly proportional to the number (noted as N_a) of dislocations at the pileup tip if N_a is less than 10, but can "upper bend" to a very high level when then of dislocations arrive at the tip (Fig. B.2c). As such, the dislocation pileup-induced internal stress concentration might have been underestimated if one only relies on nanoscale MD simulations which can only accommodate a few dislocations in the computational cell;

(4) When the pre-sheared material sample is subjected to a compression, PTs and twinning occur ahead of the dislocation pileup through a two-step process: (a) the square phase transforms to the hexagonal phase. During such a square-to-hexagonal PT (also referred as the direct PT), two variants of the hexagonal phase simultaneously nucleate, grow, contact, and form a twin boundary in between; (b) at a later stage, a portion of the newly formed hexagonal phase transforms back to the square phases. The newly formed square phase resulting from this reverse PT is found to be twinned with respect to the original square lattices and relax the local internal stresses. This is the first direct observation of twinning formation from a dislocation slip-assisted PTs and reverse PTs during monotonous loading.

(5) The Eshelby driving forces at all the newly formed PBs or TBs are zero, confirming that all of them are in the thermodynamic equilibrium. Although such analysis was performed previously in the nano- and microscale PFAs at the continuum level, it was demonstrated for the first time at atomic level. This can be an evidence of the consistency between the atomistic and continuum thermodynamic treatments in our model.

(6) The direct PT largely relaxes the local stress concentration, and the step at the slip-interface intersection is found to disassociate into multiple mini-steps (See Fig. B.3). The reverse PT then starts and the mini-steps eventually emerge as one step.

(7) The critical compressive stress, σ_c, required for initiating the PT, largely decreases with the increase of the internal stress intensity factor. Our simulations suggest a possibility of reducing σ_c for PT by a factor of 5.5 and even higher through injecting a considerably large number of dislocations into a micron-sized material sample, as observed in experiments for various material systems.

These findings highlight: **(a)** the insufficiency of only using nanoscale MD simulations to interpret the experimental observations on the slip-interface reaction, which may have involved hundreds of μm-long dislocations participating in the formation of a pileup; and **(b)** the possibility of using CAC to predict how the microscale dislocation-mediated plastic flow reacts with the buried interfaces in a variety of multi-phase materials, such as fcc/bcc, fcc/hcp, bcc/hcp metallic composites, Ti-/Zr-/high entropy alloys, among others, when subjected to a severe deformation. In such scenarios, the CAC simulation tool may provide researchers with suitable, if not the best, vehicle for simultaneously considering the microscale plasticity together with the atomic-scale interface structure relaxation. Nevertheless, this framework is considered to be still at a preliminary stage because:

(i) Comparing with MD, the length scale of the present CAC models is indeed one step closer but is not the same level as that in experiments yet. In particular, as far as the phase growth after the slip-interface reactions are concerned, a further length scaling up to microns through a CG description of the PTs in the material domain far away from the interface is needed. Otherwise, the growth of new phases from CAC simulations is confined at the nanoscale; **(ii)** In addition to the local stress, another factor that plays a vital role in the PT process is the thermal-induced atomic fluctuations. The implementation of a finite temperature algorithm into CAC for capturing the finite-temperature effects on dislocations, PTs, and their interactions is needed, especially when the correlation between phonon instability and PTs becomes a concern; **(iii)** The material system under consideration here is oversimplified in terms of crystal structure, chemistry, interatomic potential, and microstructure. A transfer of the present model or the gained knowledge for understanding the dislocations-interface reactions and subsequent structural changes in realistic multi-phase materials is not trivial. It demands: (1) the design of new finite elements for simultaneously accommodating dislocations and PTs; (2) the implementation of more sophisticated or machine learning-based interatomic potential to be trained from *ab initio* data for capturing more phase variants, as well as (3) the incorporation of realistic structures and chemistry at the GBs, PBs, and other interfaces in the materials. An expansion of CAC along those three directions and its applications in predicting the slip-interface reactions in real materials are being attempted and will be reported in the future.

CRediT authorship contribution statement

Yipeng Peng: Methodology, Software, Formal analysis, Investigation, Data curation, Writing – original draft, Writing – review & editing, Visualization . **Rigelesaiyin Ji:** Methodology, Software, Investigation, Data curation, Writing – review & editing, Visualization. **Thanh Phan:** Methodology, Software, Investigation, Data curation, Writing – review & editing. **Laurent Capolungo:** Conceptualization, Formal analysis, Resources, Writing – review & editing, Supervision, Project administration, Funding acquisition. **Valery I. Levitas:** Conceptualization, Formal analysis, Resources, Writing – review & editing, Visualization, Supervision, Project administration, Funding acquisition. **Liming Xiong:** Conceptualization, Methodology, Software, Formal analysis, Resources, Data curation, Writing – original draft, Writing – review & editing, Visualization, Supervision, Project administration, Funding acquisition.

Declaration of competing interest

The authors declare that they have no known competing financial interests or personal relationships that could have appeared to influence the work reported in this paper.

Data availability

The raw data (computational source code together with the inputs) required to reproduce these findings are available to download from https://github.ncsu.edu/tphan4/CAC.git.

Acknowledgments

YP, RJ, TP, and LX acknowledge the support of the U.S. National Science Foundation (CMMI-2322675 and CMMI2328533) and the Extreme Science & Engineering Discovery Environment (XSEDE-TG-MSS170003, XSEDE-TGMSS190008, and XSEDE-TG-MSS190013). LC acknowledge support from the U.S. Dept. of Energy, Office of Basic Energy Sciences Project FWP 06SCPE401. YP and LC also acknowledge the support

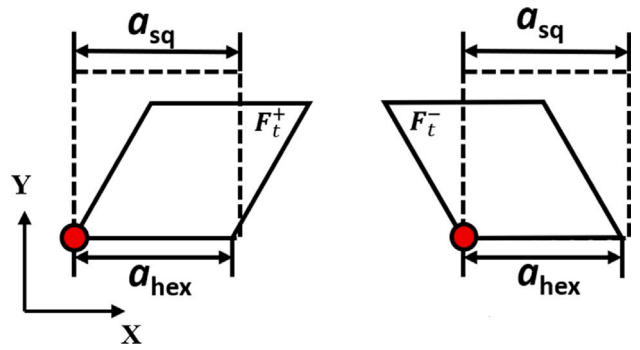

Fig. A.1. Two crystallographically equivalent variants (F_t^+ and F_t^- of hexagonal phase (solid lines) and their orientation with respect to a square phase (dash lines).

of NSF and Los Alamos National Laboratory through a NSF INTERNSHIP program under DMR-1807545. VIL work was funded by NSF (DMR2246991 and CMMI-1943710) and the ISU (Vance Coffman Faculty Chair Professorship), as well as XSEDE, allocation TG-MSS170015.

Appendix A. PT variants

Figure A.1 shows the unit cell of the square (dash lines) and the hexagonal (solid lines) phases with their lattice parameters being noted as a_{sq} and a_{hex}, respectively. In a 2D set-up, the transformation deformation gradient tensor $\boldsymbol{F}_t$, the stress and strain tensors can be all written as 2 × 2 matrices in a cartesian system with orthogonal unit basis vectors. Clearly, there are two crystallographically equivalent variants for the hexagonal phase due to the lattice symmetry. These two variants are in a twinned configuration with respect to each other.

According to the lattice cell set-up of these two phases in Fig. A.1, the transformation deformation gradient associated with those two variants resulting from the square-to-hexagonal PTs are:

$$\boldsymbol{F}_t^+ = \begin{pmatrix} 0.941 & 0.471 \\ 0 & 0.815 \end{pmatrix}; \quad \boldsymbol{F}_t^- = \begin{pmatrix} 0.941 & -0.471 \\ 0 & 0.815 \end{pmatrix}. \tag{A.1}$$

The transformation deformation gradient can be then decomposed into orthogonal and symmetric parts through $\boldsymbol{F}_t = \boldsymbol{R} \cdot \boldsymbol{U}$. The symmetric part is: $\boldsymbol{U}_t = \left(\boldsymbol{F}_t^T \cdot \boldsymbol{F}_t\right)^{1/2}$. Here the superscript T means transposition. As such, the symmetric (rotation-free) transformation deformation gradient for these two variants can be calculated as

$$\boldsymbol{U}_t^+ = \begin{pmatrix} 0.909 & 0.244 \\ 0.244 & 0.909 \end{pmatrix}; \quad \boldsymbol{U}_t^- = \begin{pmatrix} 0.909 & -0.244 \\ -0.244 & 0.909 \end{pmatrix}. \tag{A.2}$$

Appendix B. Pileup induced stress intensity factors and their evolution during PT

To characterize the stress profile ahead of the pileup tip, we construct a series of finite-sized volume elements ahead of the slip-interface intersection (see the inset picture in Fig. B.1). Each volume element is at a resolution of 5 Å × 5 Å. The stress associated with each volume element can be then calculated using the Virial formula. Fig. B.1 presents the CAC- and MD simulation-predicted shear stress distributions ahead of the dislocation pileup tip. Two major observations are: (a) both CAC and MD simulations predict an obvious stress concentration at the pileup tip and its rise upon an increase of the applied shear, τ_{ap}; (b) this stress concentration decays away from pileup tip but spans a longer range (100 nm, Fig. B.1a) in CAC than that (60 nm, Fig. B.1b) in MD because more dislocations have been piled up in the CAC model. It suggests that, similar to what has been observed in experiments [55], the participation of a large number of dislocations in a slip may produce a long-range internal stress field, which can span tens of microns away from the pileup tip if tens of dislocations are piled up.

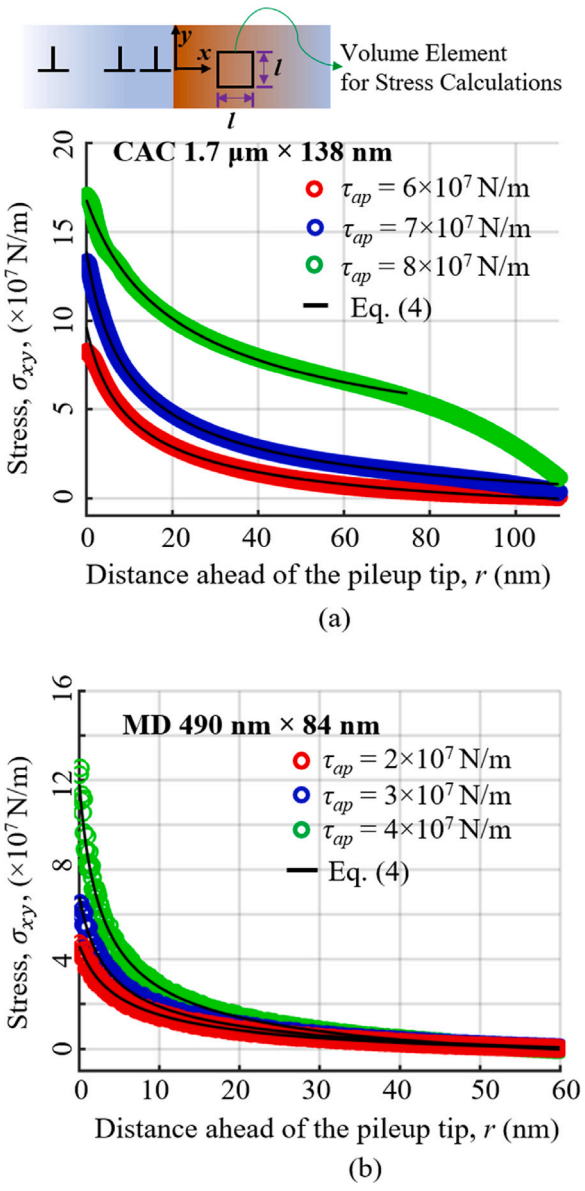

Fig. B.1. The local stress profile ahead of the slip-interface intersection under a variety of τ_{ap} from (a) CAC and (b) MD simulations and their fits into Eq. (B.1).

The obtained stress profile ahead of the pileup tip can be then fit into an equation as follows:

$$\tau_{xy} = \frac{K_b}{\sqrt{\pi(r+r_0)}} + \frac{z\mu N_a b}{2\pi(1-\upsilon)(r+r_0)} + \tau_0. \tag{B.1}$$

In this equation, the dislocation pileup-induced internal stresses is, for the first time, decomposed into two parts. The first term on the right side of Eq. (B.1) is based on the Eshelby model for the dislocations behind the pileup tip which considers the interface as a rigid obstacle to dislocation motion. The second term on the right side of Eq. (B.1) is caused by the step, also noted as the super-dislocation at the pileup tip. In Eq. (B.1), $\mu = 35.4 \times 10^7$ N/m and is the shear modulus of the materials (the hexagonal lattice in this work); b is the magnitude of the Burgers vector 2.56 Å; $\upsilon = 0.3$ and is the Poisson's ratio; N_a is the number of dislocations that participate the step formation at the pileup tip; τ_0 is a parameter for considering the uncertainty associated with the reference stress state when no dislocation is introduced in the model; r_0 is the fitting parameter due to the structural change during the step formation, the value of which suggests the location of the maximum

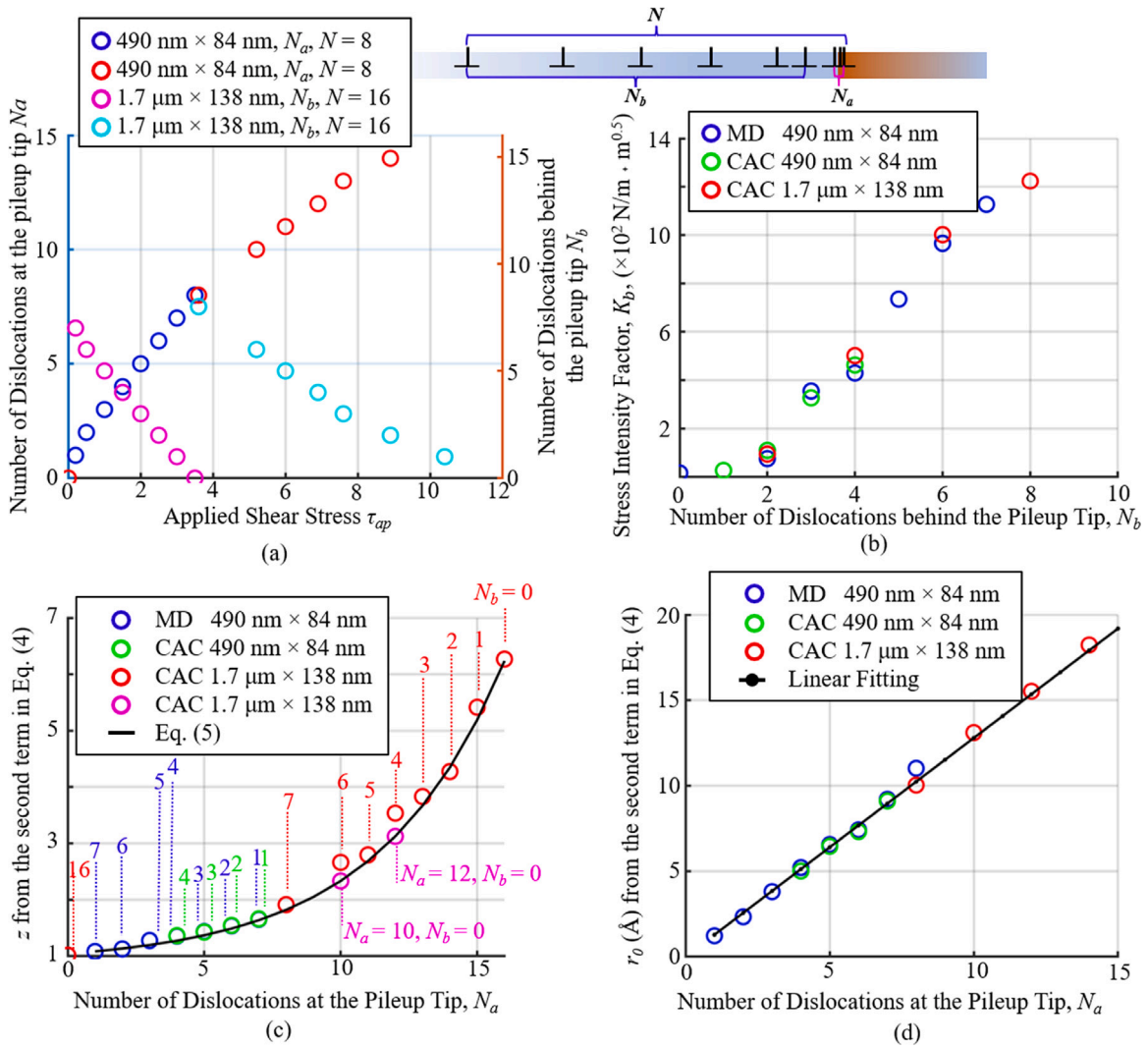

Fig. B.2. The nanoscale MD and microscale CAC simulation-predicted relationship: (a) the number of dislocations behind the pileup tip N_b, the number of dislocations at the pileup tip N_a versus the applied shear stress τ_{ap}; (b) between the internal stress intensity factor, K_b, and the number of the dislocations, N_b, behind a dislocation pileup tip; (c) between the correction coefficient z and the number of the dislocations at the dislocation pileup tip N_a; (d) between the location of the maximum internal stress, r_0, and the number of the dislocations, N_a, at the dislocation pileup tip.

internal stress at the pileup tip; r is the distance between the pileup tip and the stress measurement site; K_b is the stress intensity factor induced by the dislocations behind the pileup tip; z is the correction coefficient due to finite strain, nonlinear anisotropic elasticity, finite step size, and two-phase material.

A determination of those parameters is accomplished through fitting Eq. (B.1) into the stress profiles from two sets of simulations: (i) in simulation set-1, for a sample containing N dislocations, we apply a stress until all dislocations arrive at the interface and form a step, i.e., $N_a = N$ and $N_b = 0$. Here, N_b stands for the number of the dislocations behind the pileup tip (see inset picture of Fig. 6 for the physical meaning of N, N_a, and N_b). When $N_a = N$ and $N_b = 0$, the first term on the right side of Eq. (B.1) simply goes to zero. A fitting of simulation-based stress profile into Eq. (B.1) leads to a determination of the value of z, τ_0, and r_0; (ii) in simulation set-2, a stress lower than that in set-1 is imposed on the same sample containing N dislocations. In this situation, $N_b \neq 0$ and $N_a = N - N_b$. As such, the first term on the right side of Eq. (B.1) is non-zero. The K_b in it can be then determined by fitting the stress profile from simulation set-2 into Eq. (B.1). It should be noted that, at this step, the values of z, τ_0, and r_0 fitted from simulation set-1 are used. In the fitting process, we only consider the stress profile up to $r = 67$ nm where the internal stress does not relax due to the presence of free surfaces. Two different sample sizes are considered here. One is of a dimension of 490 nm × 84 nm and contains 8 dislocations. The other is of a dimension of 1.7 μm × 138 nm and contains 16 dislocations.

The $\tau_{ap} - N_a$ and $\tau_{ap} - N_b$ relations obtained from the MD together with CAC simulation of the dislocation pileup process are presented in Fig. B.2a. It is seen that, in all simulations, when a pileup happens upon an increase of τ_{ap}, N_a increases and N_b decreases. Fig. B.2b presents the simulation-predicted relationship between K_b and N_b. Clearly, K_b linearly increases upon an increase of N_b. In addition to K_b, another parameter that we have introduced into Eq. (B.1) is the correction coefficient z, which is needed here because: (1) the classical super-dislocation model only considers the defect embedded in an isotropic medium with a constant shear modulus of μ while we have considered the super-dislocation at a PB in a two-phase anisotropic material; (2) during the dislocation pileup process, both physical and geometric non-linearities develop; (3) additivity of stress field from each dislocation is violated. Especially, when more than 8 dislocations arrive at the PB, the slope of $z - N_a$ relation is significantly larger than that when N_a is less than 8 (Fig. B.2c). This in turn, implies that the stress intensity factor upper bends to a very high level when tens of dislocations participate the formation of a pileup at the microscale, comparing with that when

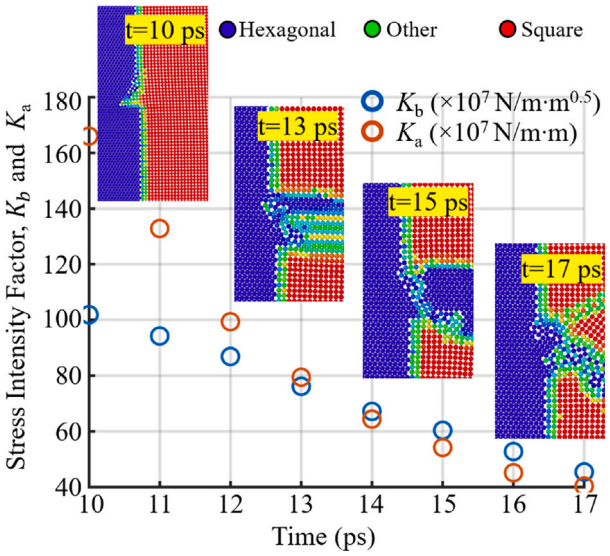

Fig. B.3. The time evolution of the stress intensity factors, K_b and K_a, ahead of the dislocation pileup tip with the inset pictures showing the snapshots of the local atomic structure changes during the direct and then reverse PTs.

only several dislocations are involved in the formation of a pileup at the nanoscale. Such a highly non-linear $z - N_a$ relation can be fit into an equation as:

$$z = 0.1656e^{0.2173N_a} + 0.8777. \tag{B.2}$$

It should be noted that the data in Fig. B.2c exhibits a trend of deviating from Eq. (B.2) when N_b is larger than 2, especially when $N = 16$, $N_a = 12$, $N_b = 4$ or when $N = 16$, $N_a = 10$, $N_b = 6$. We believe this deviation is caused by a fundamental difference between a super-dislocation model and the computer set-up for non-zero N_b. A super-dislocation model, i.e., the second term on the right side of Eq. (B.1), is only exact when $N_b = 0$, i.e, all the dislocations arriving at the interface participate the formation of a step. When N_b is larger than 2, one cannot rely on the super-dislocation model to estimate the internal stresses ahead of a slip-interface intersection any more. To confirm this assertion, we perform two additional CAC simulations. In one simulation, $N = 12$, $N_a = 12$, and $N_b = 0$. By contrast, in another simulation, $N = 10$, $N_a = 10$, and $N_b = 0$. Comparing with the data from simulations with $N = 16$, $N_a = 12$, and $N_b = 4$ or $N = 16$, $N_a = 10$, and $N_b = 6$, the results (pink circles) from these two new sets of simulations with $N_b = 0$ obviously fits into the Eq. (B.2) with a significantly less error. Other than z and K_b, another key parameter in Eq. (B.1) is r_0, which indicates the location of the maximum stress concentration. This location obviously changes during the pileup process. r_0 is thus introduced in Eq. (B.1) to capture the such local structure evolution at the pileup tip. As expected, the values of r_0 obtained from fitting simulation data into Eq. (B.1) are found to be linearly proportional to the number of the dislocations arriving at the interface (Fig. B.2d) with the slope equals to $b/2$, b as the length of the Burgers vector. This means that r_0 is located in the middle of a step produced by dislocations at the interface.

During compression, accompanied by the direct and reverse PTs, the local stresses ahead of the dislocation pileup evolves. To characterize the full complexity of such a complex internal stress evolution, we measure the local stresses and again decompose it into two parts:

$$\tau_{xy} = \frac{K_b}{\sqrt{\pi(r + r_0)}} + \frac{K_a}{(r + r_0)} + \tau_0, \tag{B.3}$$

in which K_b and K_a are noted as the intensity factors based on the Eshelby and super-dislocation model, respectively. During the process of the direct and reverse PT, a series of stress profiles ahead of the pileup tip are produced. A fitting of each stress profile into the above equation leads to a determination of the instantaneous K_b and K_a. A time evolution of K_b and K_a together with the snapshots of the atomic structure at the pileup tip are presented in Fig. B.3. Obviously, before the occurrence of PT, both K_b and K_a are at a relatively high

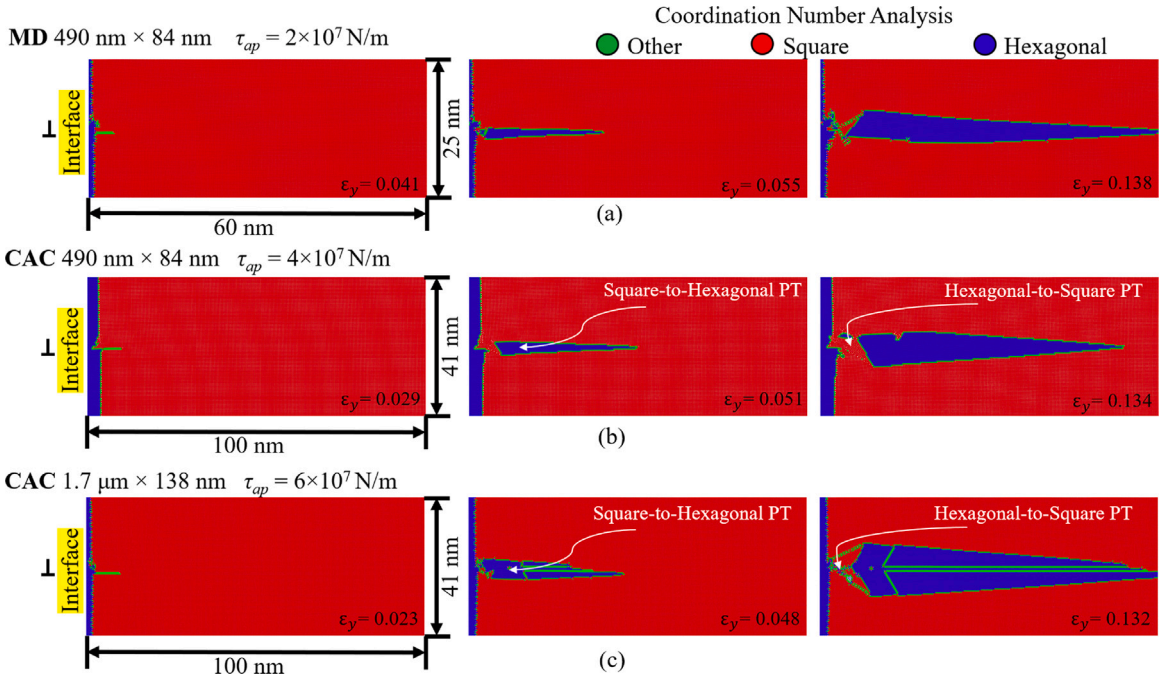

Fig. C.1. The snapshots of the atomic-scale structure evolution ahead of a slip-interface intersection showing the process of a square-to-hexagonal PT and then a reverse PT, i.e., the hexagonal-to-square PT, in a two-phase materials under a combined compression and shear through the coordination number analysis of the results from (a) MD simulations with $\tau_{ap} = 2\times10^7$ N/m; (b) CAC simulations with $\tau_{ap} = 4\times10^7$ N/m; and (c) CAC simulations with $\tau_{ap} = 6\times10^7$ N/m.

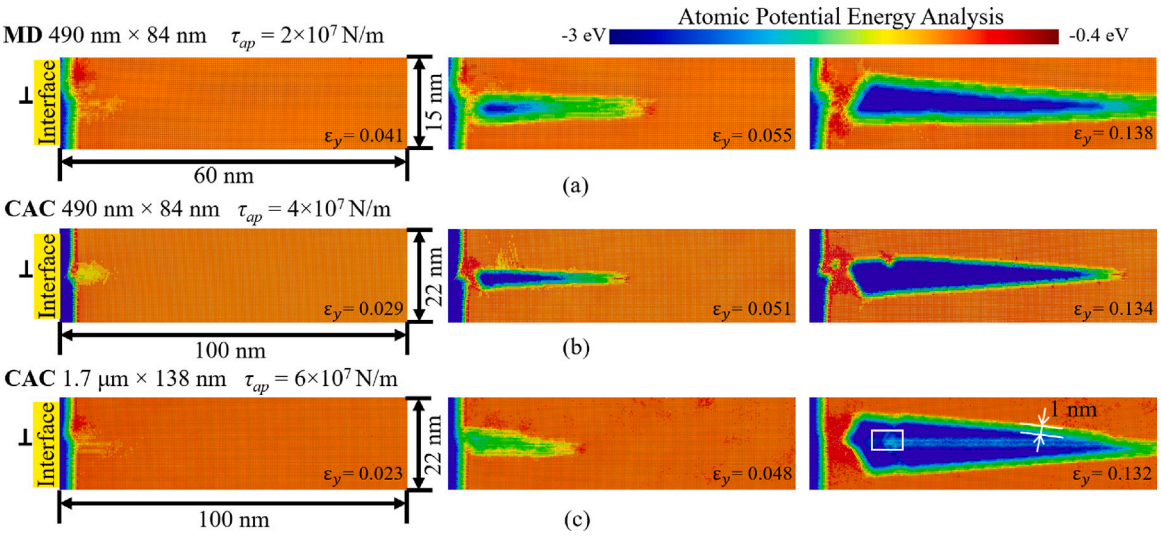

Fig. C.2. The snapshots of the atomic-scale structure evolution ahead of a slip-interface intersection showing the process of a square-to-hexagonal PT near a pileup tip in two-phase materials under a combined compression and shear through a potential energy analysis of the results from MD simulations with $\tau_{ap} = 2\times10^7$ N/m; (b) CAC simulations with $\tau_{ap} = 4\times10^7$ N/m; and (c) CAC simulations with $\tau_{ap} = 6\times10^7$ N/m.

level. And the stress intensity, K_a, induced by the dislocation at the pileup tip is larger than that, K_b, induced by the dislocations behind the pileup tip. Both K_b and K_a decrease when PTs occur. In details, at t = 13 ps, with the growth of the hexagonal phase, K_a decreases from 165 to 80 while K_b decreases from 100 to 75 (all in a unit of 10^7 N/m$^{1/2}$). It suggests that a direct PT largely relaxes the local stress concentration. Thereafter, the step at the slip-interface intersection is found to disassociate into multiple mini-steps. At this stage, the reverse PT starts and those mini-steps eventually emerge as a single step at t = 15 ps. Up to this moment, the stress intensity becomes low. At t = 14 ps, there is a cross-over of the stress intensity induced by the dislocations behind the pileup tip: K_b becomes larger than that, K_a, induced by the dislocations at the pileup tip.

Appendix C. Atomic-scale structure evolution during phase transformation

Here the CAC simulation results, especially the material microstructure evolution ahead of the dislocation pileup, are also compared with that from MD simulations. In details, Fig. C.1a shows the snapshots of atomic structure evolution from MD simulations of the deformation behavior in a sample under a pre-shear of $\tau_{ap} = 2\times10^7$ N/m together with a compressive strain of ε_y being increased from 0.054 to 0.080. In parallel, Fig. C.1b presents the results from a coordinate number analysis of the CAC simulations under $\tau_{ap} = 4\times10^7$ N/m together with ε_y increasing from 0.042 to 0.063. Fig. C.1c shows the results from CAC simulations of the dislocation pileup-assisted PT in a micron-sized sample under $\tau_{ap} = 6\times10^7$ N/m with ε_y being increased from 0.028 to 0.039. In Fig. C.1a–c, the atoms in hexagonal and square phases are colored in blue and red, respectively. The atoms in any other configuration different from hexagonal and square lattice are colored in green. They represent either the PBs that separate the hexagonal and square phase, or the stacking faults/defects in the hexagonal phases. Similar atomic structure evolution in the same region from MD (Fig. C.1a) and CAC (Fig. C.1b and c) simulations is also analyzed in terms of atomic potential energy (PE) as shown in Fig. C.2, where the atoms in hexagonal and square phases are colored in blue and orange, respectively, while those atoms with PE values deviating from the hexagonal or square lattice are in green.

Our major observations from Figs. C.1 and C.2 are: **(1)** the square-to-hexagonal PT occurs at $\varepsilon_y = 0.028$ when $\tau_{ap} = 6\times10^7$ N/m is applied on a micron-sized CAC model where tens of dislocations participate the pileup, while $\varepsilon_y = 0.054$ when $\tau_{ap} = 2\times10^7$ N/m is applied on nanoscale MD models where only a few dislocations participate the pileup; **(2)** in both CAC and MD simulations, the PT starts at the dislocation pileup tip. The newly nucleated hexagonal phase then grows into a wedge shape. Such a wedge-shape in the product phase resulting from a dislocation-assisted PT has also been observed in experiments [111], although in a different material; **(3)** the width of the interface between the parent and the product phases can be approximately estimated to be about 1 nm in both CAC and MD simulations; This value can be used for calibrating the PFA models in [50–52]; **(4)** the stacking fault in the product hexagonal phase only appears in the microscale CAC simulations at $\tau_{ap} = 6\times10^7$ N/m, suggesting an increased microstructure complexity when more dislocations are piled up.

References

[1] K. Masuda, T. Shimada, T. Kitamura, Dynamical topology in ferroelectric nanostructures by 1/2 [1$\bar{1}$0](110) dislocations in $SrTiO_3$, Phys. Rev. B 103 (5) (2021) 054114.

[2] V. Turlo, T.J. Rupert, Linear complexions: Metastable phase formation and coexistence at dislocations, Phys. Rev. Lett. 122 (12) (2019) 126102.

[3] N. Gunkelmann, E.M. Bringa, K. Kang, G.J. Ackland, C.J. Ruestes, H.M. Urbassek, Polycrystalline iron under compression: Plasticity and phase transitions, Phys. Rev. B 86 (14) (2012) 144111.

[4] N. Amadou, T. de Resseguier, A. Dragon, E. Brambrink, Coupling between plasticity and phase transition in shock- and ramp-compressed single-crystal iron, Phys. Rev. B 98 (2018) 024104.

[5] L. Capolungo, I.J. Beyerlein, Nucleation and stability of twins in HCP metals, Phys. Rev. B 78 (2) (2008) 024117.

[6] D.E. Spearot, L. Capolungo, C.N. Tomé, Shear-driven motion of Mg {10$\bar{1}$2} twin boundaries via disconnection terrace nucleation, growth, and coalescence, Phys. Rev. Mater. 3 (5) (2019) 053606.

[7] V.I. Levitas, S.E. Esfahani, I. Ghamarian, Scale-free modeling of coupled evolution of discrete dislocation bands and multivariant martensitic microstructure, Phys. Rev. Lett. 121 (20) (2018) 205701.

[8] M. Arul Kumar, M. Wroński, R.J. McCabe, L. Capolungo, K. Wierzbanowski, C.N. Tomé, Role of microstructure on twin nucleation and growth in HCP titanium: A statistical study, Acta Mater. 148 (2018) 123–132.

[9] K.K. Pandey, V.I. Levitas, In situ quantitative study of plastic strain-induced phase transformations under high pressure: Example for ultra-pure Zr, Acta Mater. 196 (2020) 338–346.

[10] V.I. Levitas, M. Javanbakht, Phase-field approach to martensitic phase transformations: Effect of Martensite–Martensite interface energy, Int. J. Mater. Res. 102 (6) (2011) 652–665.

[11] V.I. Levitas, High-pressure phase transformations under severe plastic deformation by torsion in rotational anvils, Mater. Trans. 60 (7) (2019) 1294–1301.

[12] Y. Peng, L. Xiong, Atomistic computational analysis of the loading orientation-dependent phase transformation in graphite under compression, JOM - J. Miner. Metal. Mater. Soc. 71 (11) (2019) 3892–3902.
[13] J. Liu, Q. Feng, X. Fang, H. Wang, J. Lu, D. Raabe, W. Yang, Dislocation activities at the martensite phase transformation interface in metastable austenitic stainless steel: An in-situ TEM study, Mater. Sci. Eng. A 703 (2017) 236–243.
[14] H. Zhao, M. Song, S. Ni, S. Shao, J. Wang, X. Liao, Atomic-scale understanding of stress-induced phase transformation in cold-rolled Hf, Acta Mater. 131 (2017) 271–279.
[15] V.I. Levitas, Thermomechanical theory of martensitic phase transformations in inelastic materials, Int. J. Solids Struct. 35 (9–10) (1998) 889–940.
[16] V.I. Levitas, Structural changes without stable intermediate state in inelastic material. Part I. General thermomechanical and kinetic approaches, Int. J. Plast. 16 (7–8) (2000) 805–849.
[17] V.I. Levitas, Structural changes without stable intermediate state in inelastic material. part II. Applications to displacive and diffusional–displacive phase transformations, strain-induced chemical reactions and ductile fracture, Int. J. Plast. 16 (7–8) (2000) 851–892.
[18] A.V. Idesman, V.I. Levitas, E. Stein, Elastoplastic materials with martensitic phase transition and twinning at finite strains: Numerical solution with the finite element method, Comput. Methods Appl. Mech. Engrg. 173 (1–2) (1999) 71–98.
[19] A.V. Idesman, V.I. Levitas, E. Stein, Structural changes in elastoplastic material: A unified finite-element approach to phase transformation, twinning and fracture, Int. J. Plast. 16 (7–8) (2000) 893–949.
[20] V.I. Levitas, O.M. Zarechnyy, Modeling and simulation of strain-induced phase transformations under compression in a diamond anvil cell, Phys. Rev. B 82 (17) (2010) 174123.
[21] V.I. Levitas, O.M. Zarechnyy, Modeling and simulation of strain-induced phase transformations under compression and torsion in a rotational diamond anvil cell, Phys. Rev. B 82 (17) (2010) 174124.
[22] B. Feng, V.I. Levitas, W. Li, FEM modeling of plastic flow and strain-induced phase transformation in BN under high pressure and large shear in a rotational diamond anvil cell, Int. J. Plast. 113 (2019) 236–254.
[23] J. Kundin, D. Raabe, H. Emmerich, A phase-field model for incoherent martensitic transformations including plastic accommodation processes in the austenite, J. Mech. Phys. Solids 59 (10) (2011) 2082–2102.
[24] V.I. Levitas, M. Javanbakht, Advanced phase-field approach to dislocation evolution, Phys. Rev. B 86 (14) (2012) 140101.
[25] V.I. Levitas, M. Javanbakht, Phase field approach to interaction of phase transformation and dislocation evolution, Appl. Phys. Lett. 102 (25) (2013) 251904.
[26] V.I. Levitas, M. Javanbakht, Interaction between phase transformations and dislocations at the nanoscale. Part 1. General phase field approach, J. Mech. Phys. Solids 82 (2015) 287–319.
[27] M. Javanbakht, V.I. Levitas, Interaction between phase transformations and dislocations at the nanoscale. Part 2: Phase field simulation examples, J. Mech. Phys. Solids 82 (2015) 164–185.
[28] S. Ehsan Esfahani, I. Ghamarian, V.I. Levitas, Strain-induced multivariant martensitic transformations: A scale-independent simulation of interaction between localized shear bands and microstructure, Acta Mater. 196 (2020) 430–443.
[29] K. Kadau, T.C. Germann, P.S. Lomdahl, B.L. Holian, Atomistic simulations of shock-induced transformations and their orientation dependence in BCC Fe single crystals, Phys. Rev. B 72 (6) (2005) 064120.
[30] K. Kadau, T.C. Germann, P.S. Lomdahl, B.L. Holian, Microscopic view of structural phase transitions induced by shock waves, Science 296 (5573) (2002) 1681–1685.
[31] K. Wang, W. Zhu, S. Xiao, K. Chen, H. Deng, W. Hu, Coupling between plasticity and phase transition of polycrystalline iron under shock compressions, Int. J. Plast. 71 (2015) 218–236.
[32] G. Olson, M. Cohen, Dislocation theory of martensitic transformations, in: Dislocations in Solids, North-Holland, 1986, pp. 295–407.
[33] F.C. Lovey, V. Torra, Shape memory in Cu-based alloys: Phenomenological behavior at the mesoscale level and interaction of martensitic transformation with structural defects in Cu-Zn-al, Prog. Mater. Sci. 44 (3) (1999) 189–289.
[34] P. Chowdhury, H. Sehitoglu, A revisit to atomistic rationale for slip in shape memory alloys, Prog. Mater. Sci. 85 (2017) 1–42.
[35] P. Šittner, P. Sedlák, H. Seiner, P. Sedmák, J. Pilch, R. Delville, L. Heller, L. Kadeřávek, On the coupling between martensitic transformation and plasticity in NiTi: Experiments and continuum-based modelling, Prog. Mater. Sci. 98 (2018) 249–298.
[36] F.D. Fischer, M. Berveiller, K. Tanaka, E. Oberaigner, Continuum mechanical aspects of phase transformations in solids, Arch. Appl. Mech. 64 (2) (1994) 54–85.
[37] V.I. Levitas, Continuum mechanical fundamentals of mechanochemistry, in: Y. Gogotsi, V. Dominich (Eds.), High-Pressure Surface Science and Engineering. Section 3, Institute of Physics, Bristol and Philadephia, 2004, pp. 161–292.
[38] V.I. Levitas, Phase transformations, fracture, and other structural changes in inelastic materials, Int. J. Plast. 140 (2021) 102914.
[39] P.W. Bridgman, Shearing Phenomena At High Pressures, Particularly in Inorganic Compounds, Harvard University Press, 2013.
[40] P.W. Bridgman, The effect of high mechanical stress on certain solid explosives, J. Chem. Phys. 15 (5) (1947) 311–313.
[41] V.D. Blank, E.I. Estrin, Phase Transitions in Solids under High Pressure, Crc Press, 2013.
[42] K. Edalati, S. Toh, Y. Ikoma, Z. Horita, Plastic deformation and allotropic phase transformations in Zirconia ceramics during high-pressure torsion, Scr. Mater. 65 (11) (2011) 974–977.
[43] B.B. Straumal, A.R. Kilmametov, I.A. Mazilkin, A. Korneva, P. Zieba, B. Baretzky, Phase transformations in copper–tin solid solutions at high-pressure torsion, Sov. J. Exper. Theor. Phys. Lett. 110 (9) (2020) 624–628.
[44] V.I. Levitas, L.K. Shvedov, Low-pressure phase transformation from rhombohedral to cubic BN: Experiment and theory, Phys. Rev. B 65 (10) (2002) 104109.
[45] C. Ji, V.I. Levitas, H. Zhu, J. Chaudhuri, A. Marathe, Y. Ma, Shear-induced phase transition of nanocrystalline hexagonal boron nitride to Wurtzitic structure at room temperature and lower pressure, Proc. Natl. Acad. Sci. 109 (47) (2012) 19108–19112.
[46] Y. Gao, Y. Ma, Q. An, V. Levitas, Y. Zhang, B. Feng, J. Chaudhuri, I. Goddard, Shear driven formation of nano-diamonds at sub-gigapascals and 300 K, Carbon 146 (2019) 364–368.
[47] N.V. Novikov, New trends in high-pressure synthesis of diamond, Diam. Relat. Mater. 8 (8–9) (1999) 1427–1432.
[48] V.I. Levitas, Y. Ma, E. Selvi, J. Wu, J.A. Patten, High-density amorphous phase of silicon carbide obtained under large plastic shear and high pressure, Phys. Rev. B 85 (5) (2012) 054114.
[49] V.I. Levitas, High-pressure mechanochemistry: conceptual multiscale theory and interpretation of experiments, Phys. Rev. B 70 (18) (2004) 184118.
[50] V.I. Levitas, M. Javanbakht, Phase transformations in nanograin materials under high pressure and plastic shear: Nanoscale mechanisms, Nanoscale 6 (1) (2013) 162–166.
[51] M. Javanbakht, V.I. Levitas, Phase field simulations of plastic strain-induced phase transformations under high pressure and large shear, Phys. Rev. B 94 (21) (2016) 214104.
[52] M. Javanbakht, V.I. Levitas, Nanoscale mechanisms for high-pressure mechanochemistry: A phase field study, J. Mater. Sci. 53 (19) (2018) 13343–13363.
[53] H. Chen, V. Levitas, L. Xiong, Slip of shuffle screw dislocations through Tilt grain boundaries in silicon, Comput. Mater. Sci. 157 (2019) 132–135.
[54] H. Chen, V.I. Levitas, L. Xiong, Amorphization induced by 60° shuffle dislocation pileup against different grain boundaries in silicon bicrystal under shear, Acta Mater. 179 (2019) 287–295.
[55] T.B. Britton, A.J. Wilkinson, Stress fields and geometrically necessary dislocation density distributions near the head of a blocked slip band, Acta Mater. 60 (16) (2012) 5773–5782.
[56] Y. Guo, T.B. Britton, A.J. Wilkinson, Slip band-grain boundary interactions in commercial-purity titanium, Acta Mater. 76 (2014) 1–12.
[57] L. Wang, Y. Yang, P. Eisenlohr, T.R. Bieler, M.A. Crimp, D.E. Mason, Twin nucleation by slip transfer across grain boundaries in commercial purity titanium, Metall. Mater. Trans. A 41 (2) (2010) 421–430.
[58] L. Wang, Y. Yang, P. Eisenlohr, T.R. Bieler, M.A. Crimp, D.E. Mason, Twin nucleation by slip transfer across grain boundaries in commercial purity titanium, Metall. Mater. Trans. A 41 (2) (2010) 421–430.
[59] T.R. Bieler, L. Wang, A.J. Beaudoin, P. Kenesei, U. Lienert, In situ characterization of twin nucleation in pure Ti using 3D-XRD, Metall. Mater. Trans. A 45 (1) (2014) 109–122.
[60] M.L. Martin, B.P. Somerday, R.O. Ritchie, P. Sofronis, I.M. Robertson, Hydrogen-induced intergranular failure in Nickel revisited, Acta Mater. 60 (6–7) (2012) 2739–2745.
[61] J. Kacher, B. Eftink, B. Cui, I. Robertson, Dislocation interactions with grain boundaries, Curr. Opin. Solid State Mater. Sci. 18 (4) (2014) 227–243.
[62] Z. Tarzimoghadam, D. Ponge, J. Klower, D. Raabe, Hydrogen-assisted failure in Bi-based superalloy 718 studied under in–situ hydrogen charging: The role of localized deformation in crack propagation, Acta Mater. 128 (2017) 365–374.
[63] L. Xiong, Q. Deng, G. Tucker, D.L. McDowell, Y. Chen, A concurrent scheme for passing dislocations from atomistic to continuum domains, Acta Mater. 60 (3) (2012) 899–913.
[64] L. Xiong, S. Xu, D.L. McDowell, Y. Chen, Concurrent atomistic–continuum simulations of dislocation–void interactions in FCC crystals, Int. J. Plast. 65 (2015) 33–42.
[65] S. Xu, L. Xiong, Y. Chen, D.L. McDowell, Sequential slip transfer of mixed-character dislocations across $\Sigma 3$ coherent twin boundary in FCC metals: A concurrent atomistic-continuum study, npj Comput. Math. 2 (2016) 15016.
[66] L. Xiong, D.L. McDowell, Y. Chen, Nucleation and growth of dislocation loops in Cu, Al and Si by a concurrent atomistic-continuum method, Scr. Mater. 67 (7–8) (2012) 633–636.
[67] S. Xu, L. Xiong, Q. Deng, D.L. McDowell, Mesh refinement schemes for the concurrent atomistic-continuum method, Int. J. Solids Struct. 90 (2016) 144–152.

[68] L. Xiong, X. Chen, N. Zhang, D.L. McDowell, Y. Chen, Prediction of phonon properties of 1D polyatomic systems using concurrent atomistic–continuum simulation, Arch. Appl. Mech. 84 (9) (2014) 1665–1675.
[69] S. Xu, T.G. Payne, H. Chen, Y. Liu, L. Xiong, Y. Chen, D.L. McDowell, Pycac: The concurrent atomistic-continuum simulation environment, J. Mater. Res. 33 (7) (2018) 857.
[70] H. Chen, S. Xu, W. Li, R. Ji, T. Phan, L. Xiong, A spatial decomposition parallel algorithm for a concurrent atomistic-continuum simulator and its preliminary applications, Comput. Mater. Sci. 144 (2018) 1–10.
[71] X. Chen, A. Diaz, L. Xiong, D.L. McDowell, Y. Chen, Passing waves from atomistic to continuum, J. Comput. Phys. 354 (2018) 393–402.
[72] S. Xu, L. Xiong, Y. Chen, D.L. McDowell, Validation of the concurrent atomistic-continuum method on screw dislocation/stacking fault interactions, Crystals 7 (5) (2017) 120.
[73] L. Xiong, G. Tucker, D.L. McDowell, Y. Chen, Coarse-grained atomistic simulation of dislocations, J. Mech. Phys. Solids 59 (2) (2011) 160–177.
[74] L. Xiong, Y. Chen, Coarse-grained simulations of single-crystal silicon, Modelling Simul. Mater. Sci. Eng. 17 (3) (2009) 035002.
[75] Y. Chen, S. Shabanov, D.L. McDowell, Concurrent atomistic-continuum modeling of crystalline materials, J. Appl. Phys. 126 (10) (2019) 101101.
[76] L. Xiong, Y. Chen, I.J. Beyerlein, D. McDowell, Multiscale modeling of interface-mediated mechanical, thermal, and mass transport in heterogeneous materials: Perspectives and applications, J. Mater. Res. 36 (13) (2021) 2601–2614.
[77] Y. Chen, J.D. Lee, Connecting molecular dynamics to micromorphic theory I: Instantaneous and averaged mechanical variables, Phys. A: Stat. Mech. Appl. 322 (2003) 359–376.
[78] Y. Chen, J.D. Lee, Atomistic formulation of a multiscale field theory for nano/micro solids, Phil. Mag. 85 (33–35) (2005) 4095–4126.
[79] Y. Chen, Local stress and heat flux in atomistic systems involving three-body forces, J. Chem. Phys. 124 (5) (2006) 054113.
[80] Y. Chen, Reformulation of microscopic balance equations for multiscale materials modeling, J. Chem. Phys. 130 (13) (2009) 134706.
[81] Y. Chen, A. Diaz, Local momentum and heat fluxes in transient transport processes and inhomogeneous systems, Phys. Rev. E 94 (5) (2016) 053309.
[82] Y. Chen, The origin of the distinction between microscopic formulas for stress and Cauchy stress, Europhys. Lett. 116 (3) (2016) 34003.
[83] Y. Chen, A. Diaz, Physical foundation and consistent formulation of atomic-level fluxes in transport processes, Phys. Rev. E 98 (5) (2018) 052113.
[84] J.G. Kirkwood, The statistical mechanical theory of transport processes I. General theory, J. Chem. Phys. 14 (3) (1946) 180–201.
[85] J.G. Kirkwood, The statistical mechanical theory of transport processes II. Transport in gases, J. Chem. Phys. 15 (1) (1947) 72–76.
[86] J.H. Irving, J.G. Kirkwood, The statistical mechanical theory of transport processes. IV. The equations of hydrodynamics, J. Chem. Phys. 18 (6) (1950) 817–829.
[87] R.J. Bearman, J.G. Kirkwood, Statistical mechanics of transport processes. XI. Equations of transport in multicomponent systems, J. Chem. Phys. 28 (1) (1958) 136–145.
[88] Y. Chen, A. Diaz, Physical foundation and consistent formulation of atomic-level fluxes in transport processes, Phys. Rev. E 98 (5) (2018) 052113.
[89] N. Sridharan, P. Wolcott, M. Dapino, S. Babu, Microstructure and texture evolution in aluminum and commercially pure titanium dissimilar welds fabricated using ultrasonic additive manufacturing, Scr. Mater. 117 (2016) 1–5.
[90] J. Wang, M. Knezevic, M. Jain, S. Pathak, I.J. Beyerlein, Role of interface-affected dislocation motion on the strength of Mg/Nb nanolayered composites inferred by dual-mode confined layer slip crystal plasticity, J. Mech. Phys. Solids 152 (2021) 104421.
[91] S. Zheng, I.J. Beyerlein, J.S. Carpenter, K. Kang, J. Wang, W. Han, N.A. Mara, High-strength and thermally stable bulk nanolayered composites due to twin-induced interfaces, Nature Commun. 4 (2013) 1696.
[92] I.V. Lebedeva, A.V. Lebedev, A.M. Popov, A.A. Knizhnik, Dislocations in stacking and commensurate-incommensurate phase transition in bilayer graphene and hexagonal boron nitride, Phys. Rev. B 93 (23) (2016) 235414.
[93] I.V. Lebedeva, A.M. Popov, Commensurate-incommensurate phase transition and a network of domain walls in bilayer graphene with a biaxially stretched layer, Phys. Rev. B 99 (2019) 195448.
[94] I.V. Lebedeva, A.M. Popov, Two phases with different domain wall networks and a reentrant phase transition in bilayer graphene under strain, Phys. Rev. Lett. 124 (2020) 116101.
[95] F. Cellini, F. Lavini, E. Chen, A. Bongiorno, F. Popovic, R.L. Hartman, R. Dingreville, E. Riedo, Pressure-induced formation and mechanical properties of 2D diamond boron nitride, Adv. Sci. 8 (2) (2021) 2002541.
[96] Y. Peng, F. Wang, Z. Wang, A.M. Alsayed, Z. Zhang, A.G. Yodh, Y. Han, Two-step nucleation mechanism in solid-solid phase transitions, Nature Mater. 14 (1) (2015) 101–108.
[97] J. Ruiz-Franco, J. Marakis, N. Gnan, J. Kohlbrecher, M. Gauthier, M. Lettinga, D. Vlassopoulos, E. Zaccarelli, Crytal-to-crystal transition of ultrasoft colloids under shear, Phys. Rev. Lett. 120 (2018) 078003.
[98] K.Y. Lee, J.R. Ray, Mechanism of pressure-induced martensitic phase transformations: A molecular-dynamics study, Phys. Rev. B 39 (1) (1989) 565–574.
[99] R. Gracie, T. Belytschko, Concurrently coupled atomistic and XFEM models for dislocations and cracks, Internat. J. Numer. Methods Engrg. 78 (3) (2009) 354–378.
[100] A. Koester, A. Ma, A. Hartmaier, Atomistically informed crystal plasticity model for body-centered cubic iron, Acta Mater. 60 (9) (2012) 3894–3901.
[101] S. Narayanan, D.L. McDowell, T. Zhu, Crystal plasticity model for BCC iron atomistically informed by kinetics of correlated kinkpair nucleation on screw dislocation, J. Mech. Phys. Solids 65 (2014) 54–68.
[102] Y. Peng, R. Ji, T. Phan, W. Gao, V.I. Levitas, L. Xiong, An atomistic-to-microscale computational analysis of the dislocation pileup-induced local stresses near an interface in plastically deformed two-phase materials, Acta Mater. 226 (2022) 117663.
[103] J. Wang, Atomistic simulations of dislocation pileup: Grain boundaries interaction, JOM - J. Miner. Metal. Mater. Soc. 67 (7) (2015) 1515–1525.
[104] S. Plimpton, Fast parallel algorithms for short-range molecular dynamics, J. Comput. Phys. 117 (1) (1995) 1–19.
[105] A. Stukowski, Visualization and analysis of atomistic simulation data with OVITO-the open visualization tool, Modelling Simul. Mater. Sci. Eng. 18 (1) (2010) 015012.
[106] K. Bhattacharya, S. Conti, G. Zanzotto, J. Zimmer, Crystal symmetry and the reversibility of martensitic transformations, Nature 428 (6978) (2004) 55–59.
[107] P. Castany, Y. Yang, E. Bertrand, T. Gloriant, Reversion of a parent $\{130\}\langle 310\rangle$ α'' martensitic twinning system at the origin of $\{332\}\langle 113\rangle$ β twins observed in metastable β titanium alloys, Phys. Rev. Lett. 117 (24) (2016) 245501.
[108] J. Ombogo, A.H. Zahiri, T. Ma, L. Cao, Nucleation of $\{1012\}$ twins in magnesium through reversible martensitic phase transformation, Metals 10 (8) (2020) 1030.
[109] A.H. Zahiri, J. Ombogo, L. Cao, Formation of $\{112^{-}2\}$ contraction twins in titanium through reversible martensitic phase transformation, Scr. Mater. 195 (2021) 113694.
[110] H. Babaei, V.I. Levitas, Finite-strain scale-free phase-field approach to multivariant martensitic phase transformations with stress-dependent effective thresholds, J. Mech. Phys. Solids 144 (2020) 104114.
[111] A. Ibarra, D. Caillard, J. San Juan, M. Nó, Martensite nucleation on dislocations in Cu–Al–Ni shape memory alloys, Appl. Phys. Lett. 90 (10) (2007) 101907.